



A double peak in the seasonality of California's photosynthesis as observed from space

Alexander J. Turner^{1,2,3}, Philipp Köhler⁴, Troy S. Magney^{3,4,5}, Christian Frankenberg^{3,4}, Inez Fung¹, and Ronald C. Cohen^{1,2}

¹Department of Earth and Planetary Sciences, University of California, Berkeley, CA, 94720, USA.

²College of Chemistry, University of California, Berkeley, CA, 94720, USA.

³Jet Propulsion Laboratory, California Institute of Technology, Pasadena, CA, 91109, USA.

⁴Division of Geological and Planetary Sciences, California Institute of Technology, Pasadena, CA, 91226, USA.

⁵Department of Plant Sciences, University of California, Davis, CA, 95616, USA.

Correspondence: Alexander J. Turner (alexjturner@berkeley.edu)

1 **Abstract.** Solar-Induced chlorophyll Fluorescence (SIF) has been shown to be a powerful proxy for photosynthesis and gross
2 primary productivity (GPP). The recently launched TROPospheric Monitoring Instrument (TROPOMI) features the required
3 spectral resolution and signal-to-noise ratio to retrieve SIF from space. Here we present an oversampling and downscaling
4 method to obtain 500-m spatial resolution SIF over California. We report daily values based on a 14-day window. TROPOMI
5 SIF data show a strong correspondence with daily GPP estimates at AmeriFlux sites across multiple ecosystems in California.
6 We find a linear relationship between SIF and GPP that is largely invariant across ecosystems with an intercept that is not
7 significantly different from zero. Measurements of SIF from TROPOMI agree with MODIS vegetation indices (NDVI, EVI,
8 and NIR_v) at annual timescales but indicate different temporal dynamics at monthly and daily timescales. TROPOMI SIF
9 data show a double peak in the seasonality of photosynthesis, a feature that is not present in the MODIS vegetation indices.
10 The different seasonality in the vegetation indices may be due to a clear-sky bias in the vegetation indices, whereas SIF has
11 a low sensitivity to clouds and can detect the downregulation of photosynthesis even when plants appear green. We further
12 decompose the spatio-temporal patterns in the SIF data based on land cover. The double peak in the seasonality of California's
13 photosynthesis is due to two processes that are out of phase: grasses, chaparral, and oak savanna ecosystems show an April
14 maximum while evergreen forests peak in June. An empirical orthogonal function (EOF) analysis corroborates the phase offset
15 and spatial patterns driving the double peak. The EOF analysis further indicates that two spatio-temporal patterns explain 84%
16 of the variability in the SIF data. Results shown here are promising for obtaining global GPP at sub-kilometer spatial scales
17 and identifying the processes driving carbon uptake.

18 1 Introduction

19 Photosynthesis is the process by which plants and other organisms use sunlight to synthesize carbon dioxide (CO₂) and water
20 to glucose and oxygen. Accurate knowledge of gross primary productivity (GPP) through photosynthesis is crucial for under-
21 standing the land-atmosphere carbon exchange, which is one of the largest and most uncertain aspects of the global carbon



1 cycle (IPCC, 2013; Anav et al., 2015; USGCRP, 2018). This uncertainty in the land-atmosphere carbon exchange has led to
2 long-standing questions regarding the magnitude of the Northern Hemispheric terrestrial carbon sink and how it has changed
3 over the past few decades (e.g., Tans et al., 1990; Ballantyne et al., 2012; Ciais et al., 2019). As such, more direct methods of
4 inferring GPP are of great interest to the scientific community.

5 Previous work estimating regional or global scale GPP has typically relied on either biosphere models (e.g., the early work
6 on SiB2 from Sellers et al., 1986), used remote-sensing measurements in Monteith light use efficiency models with scalings
7 for different ecosystems and climatic conditions (e.g., Monteith, 1972; Mahadevan et al., 2008), or attempted to back out GPP
8 from CO₂ flux inversions (e.g., CarbonTracker from Peters et al., 2007). The advent of global remote-sensing observations
9 of Solar-Induced chlorophyll Fluorescence (SIF) represents a breakthrough in our ability to constrain photosynthetic activity
10 from space. This is because a number of studies have shown SIF to be a powerful proxy for photosynthesis both in laboratory
11 environments (e.g., Baker, 2008) and at larger spatial scales (e.g., Frankenberg et al., 2011a; Parazoo et al., 2014; Yang et al.,
12 2015, 2017; Sun et al., 2017, 2018b; Magney et al., 2019a). During the initial stage of photosynthesis, absorbed sunlight excites
13 chlorophyll *a* molecules. The primary pathways for de-excitation are via photochemistry or non-photochemical quenching, the
14 latter of which dissipates excess energy as heat when the plant does not have the capacity for photosynthesis (i.e. under stress).
15 However, a small fraction dissipates as heat or is re-emitted as fluorescence and can be measured by remote sensing. This
16 remote sensing retrieval is termed SIF.

17 The first global space-borne measurements of SIF were made by Frankenberg et al. (2011b) and Joiner et al. (2011) using
18 observations from the Japanese GOSAT instrument (Kuze et al., 2009). Since then, SIF has been retrieved from other space-
19 borne instruments such as: GOME-2 on the METOP-A satellite, SCIAMACHY on the ENVISAT satellite, the OCO-2 satellite,
20 and TROPOMI on the Sentinel-5 Precursor satellite (Frankenberg et al., 2011a, b, 2012, 2014; Joiner et al., 2011, 2012,
21 2013, 2014, 2016; Guanter et al., 2012, 2015; Köhler et al., 2015, 2018). A number of upcoming satellite missions such
22 as FLEX (Drusch et al., 2017) and TEMPO (Zoogman et al., 2017) will also measure SIF at higher spatial and temporal
23 resolution. Efforts are underway to create a multi-decadal SIF record using different space-borne instruments (Parazoo et al.,
24 2019) and a few groups have utilized machine learning techniques to create spatially continuous SIF datasets at 0.05°×0.05°
25 resolution (Zhang et al., 2018; Yu et al., 2019; Li and Xiao, 2019). Mohammed et al. (2019) presents a detailed review of
26 different remote sensing techniques for retrieving SIF from space-borne measurements.

27 Some work has shown SIF to be a better measure of carbon uptake than other vegetation indices that look at canopy “green-
28 ness”. This is, in part, because indices like the normalized difference vegetation index (NDVI) are a measure of photosynthetic
29 capacity (Sellers et al., 1986) whereas SIF is a measure of the photosynthetic activity and is coupled to the radiation regime.
30 For example, Luus et al. (2017) showed that the seasonal cycle of a biosphere model driven by SIF agreed with measurements
31 of CO₂ whereas the seasonal cycle from the model driven by the Enhanced Vegetation Index (EVI) was markedly different
32 from the CO₂ observations. Joiner et al. (2011) showed that the seasonal cycles of SIF and EVI agree in some regions, but not
33 others. Walther et al. (2016) showed a decoupling of the photosynthesis and greenness dynamics in boreal evergreen forests
34 by comparing SIF and EVI to model estimates of GPP, with SIF better capturing the seasonality of both deciduous broadleaf
35 and evergreen needleleaf forests. Again, this is likely due to SIF capturing photosynthetic activity, rather than photosynthetic



1 capacity. More recently, Magney et al. (2019a) demonstrated a mechanistic link between SIF and GPP over the course of a
2 year in a winter-dormant Northern Hemisphere conifer forest, despite retaining chlorophyll through the winter. Magney et al.
3 (2019a) highlighted the potential for new satellite measurements of SIF from TROPOMI and OCO-2 to track GPP at coarse
4 spatial resolution ($3.5 \times 7 \text{ km}^2$).

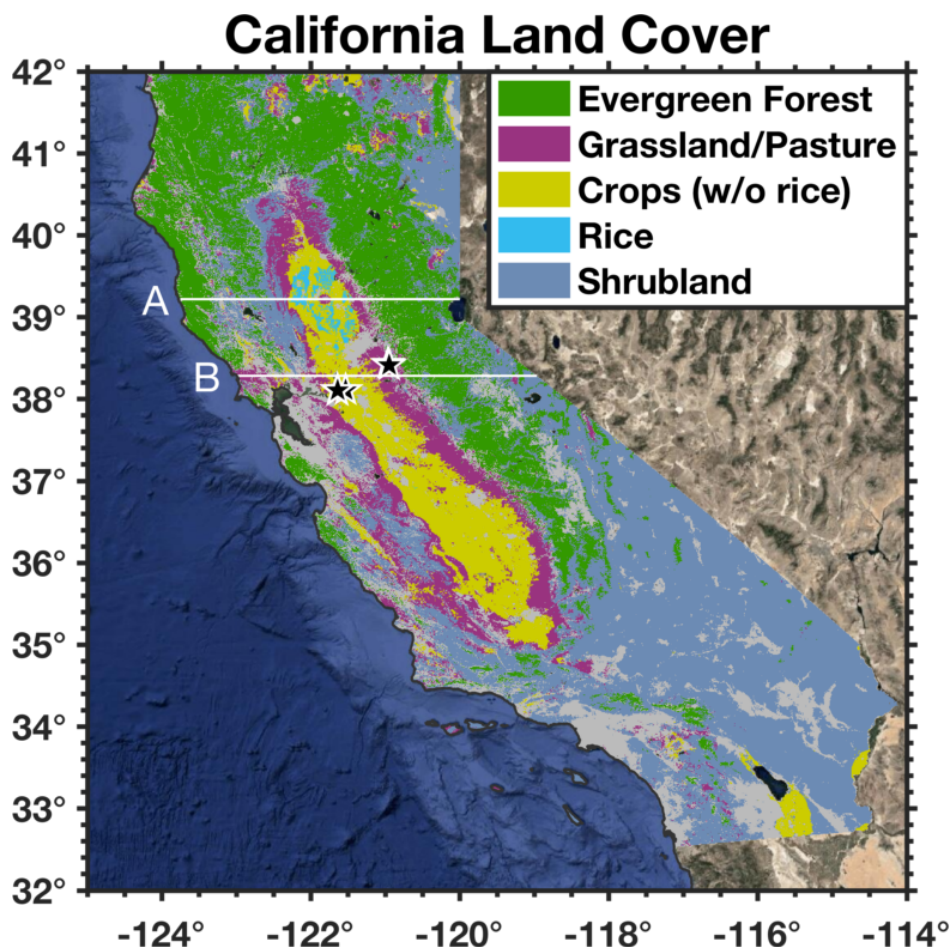


Figure 1. California land cover. Land cover in California from the 2018 USDA CropScape database (USDA, 2018). Resolution has been degraded from the native 30-m resolution to 500-m for comparison with TROPOMI data. Coloring indicates that a land type makes up more than 50% of the 500-m grid cell. White lines are the locations of two transects across California for Hovmöller diagrams: 39.218°N (Transect A), and 38.282°N (Transect B). Black stars show the location of six AmeriFlux sites: Bouldin Island (38.1090°N , 121.5350°W ; US-Bi2), Tonzi Ranch (38.4316°N , 120.9660°W ; US-Ton), Vaira Ranch (38.4133°N , 120.9507°W ; US-Var), Twitchell Island West Pond (38.1074°N , 121.6469°W ; US-Tw1), Twitchell Island East End (38.1030°N , 121.6414°W ; US-Tw4), and Twitchell Island East Pond (38.1072°N , 121.6426°W ; US-Tw5).



1 Here we present an oversampling and downscaling method to obtain daily estimates of SIF at 500-m resolution. To our
2 knowledge, this is the highest resolution SIF dataset from satellite measurements. We then compare this down-scaled 500-m SIF
3 data to AmeriFlux sites across the state of California to assess the relationship between SIF and GPP. We finish by decomposing
4 California's spatio-temporal patterns of photosynthesis and carbon uptake into the dominant modes using empirical orthogonal
5 functions (EOFs). Here we focus on California because there are a number of eddy flux towers and it encompasses a range of
6 diverse ecosystems including: deciduous and evergreen forests, irrigated croplands, and grasslands (see Fig. 1).

7 **2 Measurements of SIF, vegetation, and GPP**

8 **2.1 Satellite measurements of Solar-Induced chlorophyll Fluorescence (SIF) from TROPOMI**

9 The TROPospheric Monitoring Instrument (TROPOMI; Veefkind et al., 2012) is a nadir-viewing imaging spectrometer with
10 bands in the UV, visible, shortwave infrared, and near-infrared aboard the Sentinel-5 Precursor satellite. The Sentinel-5 Pre-
11 cursor satellite was launched into low earth orbit on October 13, 2017 with an equatorial crossing time of 13:30 local solar
12 time and a 16 day orbit cycle. TROPOMI has a wide swath (2,600 km across track) enabling near-daily global coverage. The
13 spatial resolution of the ground pixels is 7 km along track and 3.5-15 km across track (3.5 km at nadir and 15 km at the edge of
14 the swath). Of particular relevance here is the near-infrared band (725-775 nm) that covers the far-red part of SIF emission and
15 contains a number of solar absorption features in the solar irradiance (Fraunhofer lines), allowing for retrieval of SIF through
16 the change in optical depth of Fraunhofer lines. Guanter et al. (2015) showed the potential for TROPOMI to retrieve SIF and
17 Köhler et al. (2018) presented the first retrievals. Specifically, Köhler et al. (2018) used a 743-758 nm retrieval window that
18 is devoid of atmospheric absorption features. TROPOMI has a spectral resolution of ~ 0.4 nm and a signal-to-noise ratio of
19 $\sim 2,500$ in this retrieval window. The TROPOMI SIF retrieval uses a singular value decomposition to derive the spectral basis
20 functions from TROPOMI data over vegetation-free areas (e.g., oceans, ice, and deserts).

21 One particularly attractive feature of space-borne SIF retrievals is the low sensitivity to atmospheric scattering by aerosols
22 and clouds. Specifically, Frankenberg et al. (2012) showed that 80% of the emitted SIF could be retrieved in the presence of
23 clouds with low-to-moderate optical thickness. This weak sensitivity to clouds is in contrast to reflectance based measures of
24 vegetation (e.g., NDVI) that can only be made in clear-sky conditions, potentially inducing a clear-sky bias in reflectance based
25 vegetation indices.

26 Here, we apply one additional bias correction to the TROPOMI retrievals that was not included in Köhler et al. (2018). We
27 find some mostly barren regions have systematically negative SIF values, which is non-physical. This bias is thought to be
28 related to bright surfaces and is likely due to the choice of training data for the spectral basis functions. We are investigating
29 ways to correct this globally. In the interim, we compute a spatio-temporal bias correction $b_{i,j,k}$ (where i, j are the spatial
30 coordinates and k is the temporal coordinate) such that the mean SIF for a given location over a 30-day moving window is



1 always positive. That is to say,

$$2 \quad b_{i,j,k} = \begin{cases} |\bar{s}_{i,j,k}|, & \bar{s}_{i,j,k} < 0 \\ 0, & 0 \leq \bar{s}_{i,j,k} \end{cases} \quad (1)$$

3 where $\bar{s}_{i,j,k}$ is the 1-month block average for the k^{th} day at location i, j . This still allows for negative SIF values due to vari-
4 ability and noise but will shift the mean SIF for a given 500-m grid cell to be positive. In practice, this bias correction is small
5 with 78% having no bias correction at all and 89% of the grid cells having a bias correction smaller than 0.1 mW/m²/sr/nm.
6 The bias correction primarily impacts desert regions in Southeastern California (see Supplemental Fig. S1).

7 2.2 Satellite-based vegetation indices from MODIS

8 MODERate Resolution Imaging Spectroradiometer (MODIS) is an imaging spectrometer on NASA's Terra and Aqua satellites.
9 Terra launched in 2000 and Aqua launched in 2002, both are in sun-synchronous orbits with 16 orbits per day. Terra and Aqua
10 have equatorial crossing at 10:30 and 12:00 local solar time, respectively. Schaaf et al. (2002) developed the Nadir Bidirectional
11 reflectance distribution function-Adjusted Reflectance (NBAR) dataset, hereafter referred to as the MODIS NBAR dataset.
12 MODIS data over a 16-day period from Terra and Aqua can be combined to build a 500-m composite: MCD43A4. Here
13 we use the MCD43A4.006 (v06) MODIS NBAR dataset to compute three MODIS vegetation indices at 500-m resolution.
14 Specifically, we compute the normalized difference vegetation index (NDVI), enhanced vegetation index (EVI), and near-
15 infrared reflectance of vegetation index (NIR_v):

$$16 \quad \text{NDVI} = \frac{\rho_{\text{NIR}} - \rho_{\text{red}}}{\rho_{\text{NIR}} + \rho_{\text{red}}} \quad (2)$$

$$17 \quad \text{EVI} = G \cdot \frac{\rho_{\text{NIR}} - \rho_{\text{red}}}{\rho_{\text{NIR}} + C_1 \rho_{\text{red}} - C_2 \rho_{\text{blue}} + L} \quad (3)$$

$$18 \quad \text{NIR}_v = \rho_{\text{NIR}} \cdot \text{NDVI} \quad (4)$$

19 where ρ_{NIR} , ρ_{red} , and ρ_{Blue} are the reflectances in their respective MODIS bands and G , C_1 , C_2 , and L are coefficients for the
20 MODIS EVI algorithm ($L = 1$, $C_1 = 6$, and $C_2 = 7.5$, $G = 2.5$).

21 2.3 GPP estimates from AmeriFlux eddy covariance sites

22 AmeriFlux is a network of long-term eddy covariance sites that launched in 1996 (Baldocchi et al., 2001). These eddy covari-
23 ance sites provide a direct measure of net ecosystem exchange (NEE; CO₂ fluxes) (Baldocchi et al., 1988) and can be used
24 to evaluate both bottom-up models and satellite proxies of carbon exchange. Disentangling the CO₂ fluxes into GPP (CO₂
25 uptake) and total ecosystem respiration (R_{eco} ; CO₂ released) generally requires making assumptions about the temperature
26 dependence of the respiration which can induce biases in the GPP estimate (Reichstein et al., 2005). Nevertheless, these eddy
27 covariance sites provide the best estimate of site level GPP across multiple ecosystems in California including: croplands, wet-
28 lands, woody savannas, and grasslands. Here we use data from 11 AmeriFlux sites across California (see Table 1) to evaluate
29 the SIF retrievals from TROPOMI. NEE flux partitioning at these sites was performed using artificial neural networks from
30 nighttime measurements to constrain R_{eco} (Hemes et al., 2019).



Table 1. AmeriFlux sites used in this study.

Site ID	Site name	Latitude (°N)	Longitude (°W)	Elevation (m a.s.l.)	Vegetation type ^a
US-Bi1	Bouldin Island Alfalfa	38.0992	121.4993	-3	CRO ^b
US-Bi2	Bouldin Island Corn	38.1090	121.5350	-5	CRO ^b
US-EDN	Eden Landing Ecological Reserve	37.6156	122.1140	1	WET ^c
US-Myb	Mayberry Wetland	38.0499	121.7650	-4	WET ^c
US-Sne	Sherman Island Restored Wetland	38.0369	121.7547	-5	GRA ^d
US-Ton	Tonzi Ranch	38.4316	120.9660	177	WSA ^e
US-Tw1	Twitchell Island West Pond	38.1074	121.6469	-9	WET ^c
US-Tw3	Twitchell Island Alfalfa	38.1159	121.6467	-9	CRO ^b
US-Tw4	Twitchell Island East End	38.1030	121.6414	-5	WET ^c
US-Tw5	Twitchell Island East Pond	38.1072	121.6426	-5	WET ^c
US-Var	Vaira Ranch	38.4133	120.9507	129	GRA ^d

^a Vegetation classification based on the International Geosphere-Biosphere Programme (IGBP) classification scheme (Strahler et al., 1999).

^b CRO (Croplands): Lands covered with temporary crops followed by harvest and a bare soil period (e.g., single and multiple cropping systems). Note that perennial woody crops will be classified as the appropriate forest or shrub land cover type.

^c WET (Permanent Wetlands): Lands with a permanent mixture of water and herbaceous or woody vegetation that cover extensive areas. The vegetation can be present in either salt, brackish, or fresh water.

^d GRA (Grasslands): Lands with herbaceous types of cover. Tree and shrub cover is less than 10%.

^e WSA (Woody Savannas): Lands with herbaceous and other understory systems, and with forest canopy cover between 30-60%. The forest cover height exceeds 2 meters.

1 2.4 Comparison of TROPOMI SIF with MODIS vegetation indices

2 Figure 2 shows a scatterplot comparison of TROPOMI SIF and MODIS NDVI, EVI, and NIR_v. The comparison is limited to
 3 coincident observations between March and August (MAMJJA) and excludes scenes that are predominantly barren or shrub-
 4 land. A few features that immediately stand out are:

- 5 1. The strong correspondence between EVI and NIR_v. We find a nearly linear relationship between these two indices
 6 ($r^2 = 0.98$).
- 7 2. All three MODIS indices are well correlated with each other ($r^2 > 0.85$). We do observe a weakly non-linear relationship
 8 between NIR_v and EVI or NDVI (see the curvature in the NIR_v row).

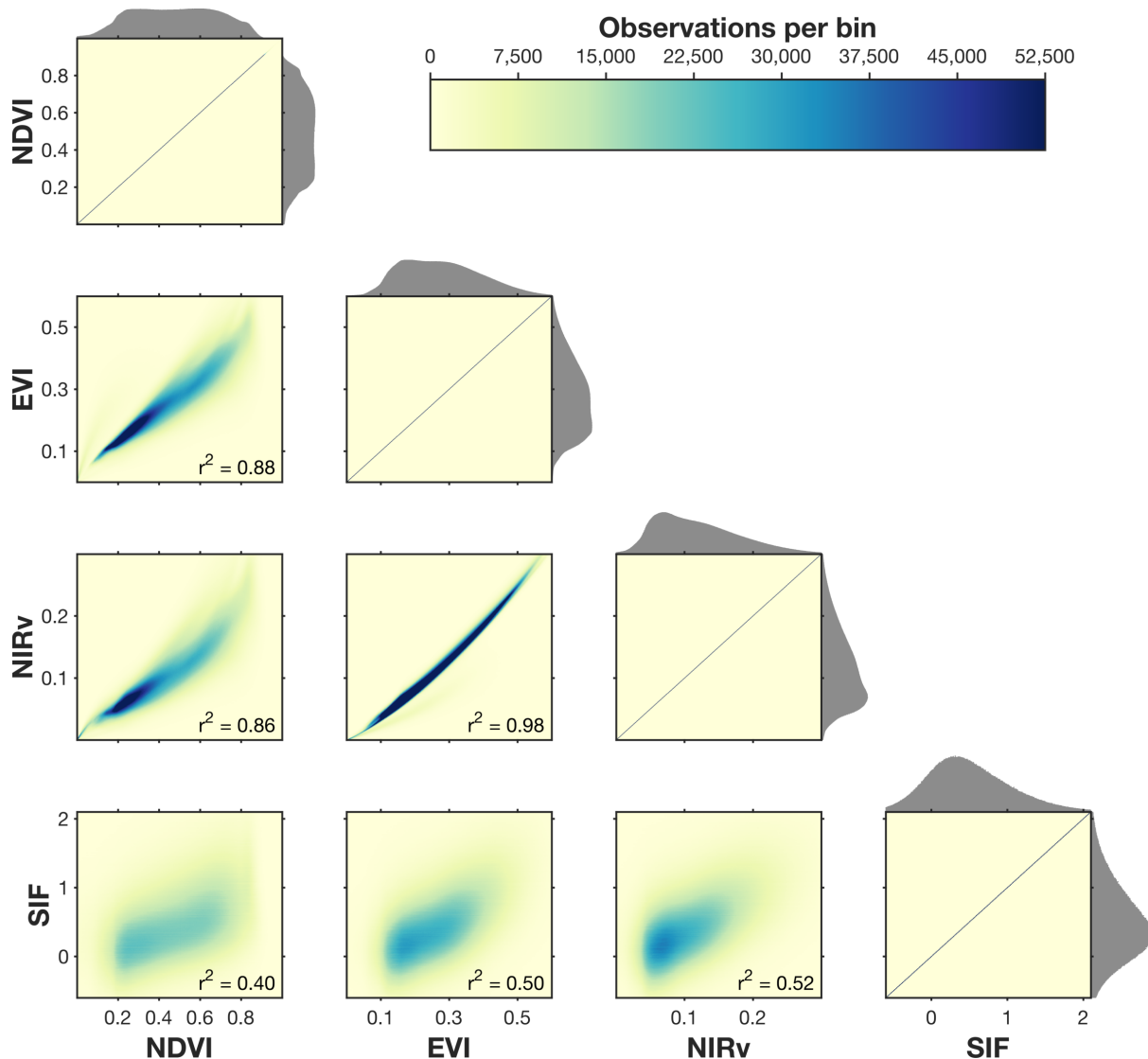


Figure 2. Comparison of MODIS vegetation indices and TROPOMI SIF from 2018-2019. Panels show a comparison of coincident measurements in both space and time of NDVI, EVI, NIR_v, and SIF. NDVI, EVI, and NIR_v use the 500-m MODIS BRDF-corrected reflectances and SIF is from TROPOMI. Shading indicates the density of points. Data is filtered to only include measurements from March through August (MAMJJA). Data is further filtered to remove scenes that are more than 85% barren or shrubland as defined by the CropScape Database. Gray histogram on the x/y-axes show the distribution of values for a given set of data. Supplemental Fig. S2 shows the comparison including the SIF downsampled using local MODIS vegetation indices.



1 3. The weaker relationship between SIF and the vegetation indices. Previous work has argued that NIR_v is strongly cor-
2 related with SIF (Badgley et al., 2017) and provides a new independent approach for estimating GPP (Badgley et al.,
3 2019).
4 Of the three vegetation indices examined here, we find the strongest relationship between NIR_v and SIF, but it only explains
5 half of the variability on daily timescales ($r^2 = 0.52$). The agreement improves at coarser temporal scales (annual $r^2 = 0.83$ –
6 0.84 and monthly $r^2 = 0.59 \pm 0.23$). It is important to note that the native spatial resolution of the TROPOMI observations
7 are 3.5-km across-track at nadir, whereas the MODIS observations are 500-m across-track at nadir. As such, we are using
8 all MODIS observations within a single TROPOMI scene. Comparison of four methods of downscaling SIF with NIR_v yield
9 coefficients of determination of $r^2 = 0.52 - 0.64$; see Fig. S2).

10 3 Oversampling and spatial-downscaling of TROPOMI data

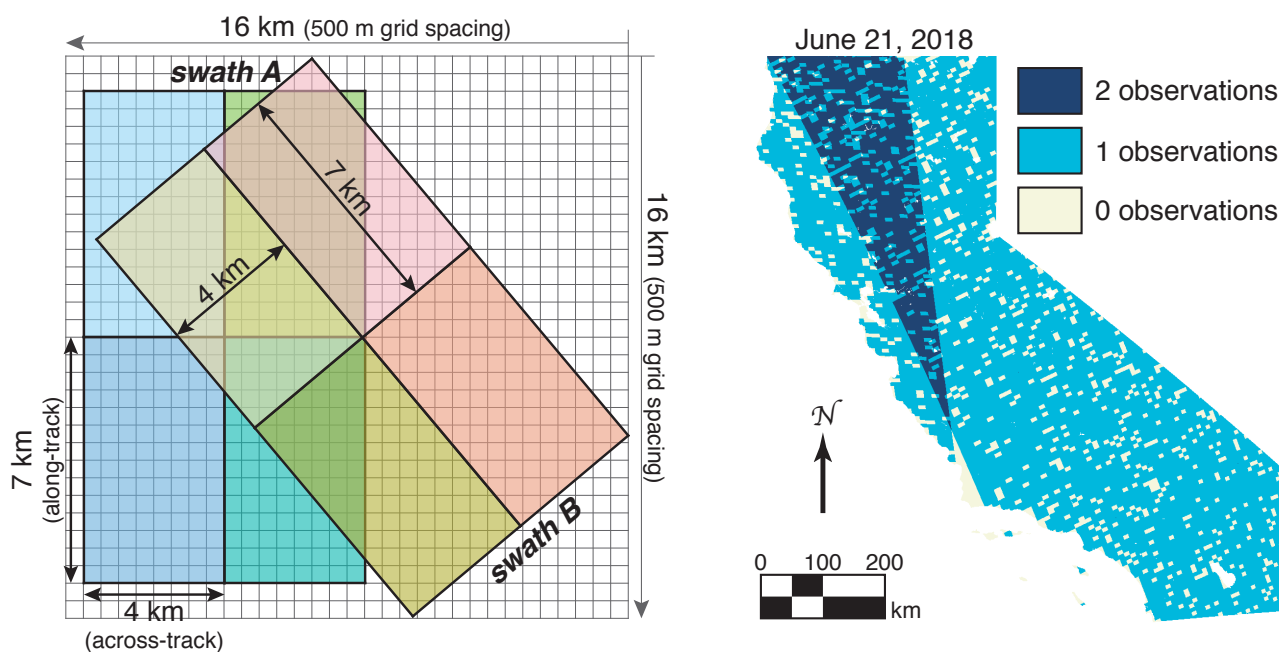


Figure 3. Oversampling schematic. Left panel shows the schematic for our oversampling. Gray grid has a grid spacing of 500 m (equivalent to the spatial resolution of the MODIS MCD43A4 product). TROPOMI ground pixels are 7 km along-track and vary from 3.5 km (at nadir) to 15 km off swath edge) across-track. Schematic shows the spatial extent of eight hypothetical TROPOMI scenes from two swaths at 7×4 km², individual TROPOMI scenes are a different color. Swath B is rotated 40° relative to swath A, resulting in overlapping pixels. Right panel shows the number of successful retrievals on June 21, 2018 over California plotted on a 500-m grid.

11 As mentioned above, the nominal spatial resolution of the ground pixels from TROPOMI are 3.5×7 km² at nadir. However,
12 the wide swath from TROPOMI (2600 km across-track) often results in multiple observations per day (see right panel of



1 Fig. 3). Additionally, the orientation of these swaths differ over the 16-day orbit cycle allowing us to infer higher spatial
2 resolution than the nominal spatial resolution. This idea has been widely used with the space-borne OMI instrument that
3 preceded TROPOMI (see Sun et al., 2018a, and references therein for a discussion of oversampling with OMI observations).
4 However, the spatial resolution of TROPOMI is a factor of 15 finer than OMI ($3.5 \times 7 \text{ km}^2$ for TROPOMI and $14 \times 26 \text{ km}^2$ for
5 OMI, both at nadir). Oversampling with OMI often required years of observations (e.g., Zhu et al., 2014). The wide swath and
6 high spatial dense spatial coverage of TROPOMI allow us to perform biweekly oversampling.

7 Fig. 3 shows a schematic of how the oversampling is performed. The left panel shows two hypothetical swaths from
8 TROPOMI overlaid on a 500-m grid (same spatial resolution as the MODIS NBAR dataset). Areas where the swaths overlap
9 allow for us to partition the information down to a finer spatial scale. For example, the yellow pixel in swath B overlaps with all
10 four pixels from swath A. As such, the signal from that pixel in swath B can be sub-divided to finer spatial scales. Each unique
11 shade of color would correspond to unique information in the left panel of Fig. 3. The right panel of Fig. 3 shows the sampling
12 density of TROPOMI over California on a single day in June 2018, the dark blue region indicates where two TROPOMI swaths
13 overlapped that day.

14 We find that, on average, each 500-m grid cell is within the bounds of ~ 0.6 TROPOMI scenes with a successful retrieval per
15 day. By using biweekly oversampling (a moving 14-day window) we obtain approximately 8 different swath orientations over
16 a 14-day period for the oversampling. These 8 swath orientations allow us to further refine our grid to following the schematic
17 shown in Figure 3. It also means that the daily values presented here are representative of 14-day moving averages (centered
18 about that day).

19 We can take the oversampling a step further by pre-weighting the SIF signal in a TROPOMI scene by the underlying
20 vegetation fraction, we refer to this as “downscaling”. That is to say, we assume the observed SIF from TROPOMI in a given
21 scene likely originates from more vegetated regions within that scene. Here we use a relative weighting for this downscaling:

$$22 \quad s_{i,j} = s^* \frac{v_{i,j}}{\bar{v}} \quad (5)$$

23 where s^* is the retrieved SIF from TROPOMI for a single scene, $s_{i,j}$ is the SIF spatially downscaled to 500-m, $v_{i,j}$ are the
24 vegetation indices from MODIS that fall within the bounds of a single scene from TROPOMI (i.e., the gray boxes within a
25 TROPOMI box in the left panel of Fig. 3), and \bar{v} is the mean vegetation index over a given TROPOMI scene. Using Eq. 5 with
26 $\mathbf{v} = [1, \dots, 1]$ returns the unweighted oversampling result. Following this, $s_{i,j}$ will naturally revert to oversampling in regions
27 with homogeneous vegetation (as inferred by MODIS).

28 Figure 4 shows the 2018 annual mean SIF from TROPOMI from Köhler et al. (2018) at $0.05^\circ \times 0.05^\circ$ spatial resolution
29 and California’s seasonal cycle at weekly temporal resolution (non-bias corrected). The middle and bottom rows of Figure 4
30 show the 2018 annual mean SIF and seasonal cycle using oversampling and spatially downscaled with NIR_v from MODIS. All
31 three show consistent large-scale spatial patterns. We do, however, find significant differences between the results from Köhler
32 et al. (2018) and the oversampling or downscaling method over the San Francisco Bay Area where the complex topography
33 induces numerical artifacts such as high SIF values over water. We also point out that the Köhler et al. (2018) seasonal cycle
34 is at weekly temporal resolution whereas we obtain daily temporal resolution because of the 14-day moving window. The

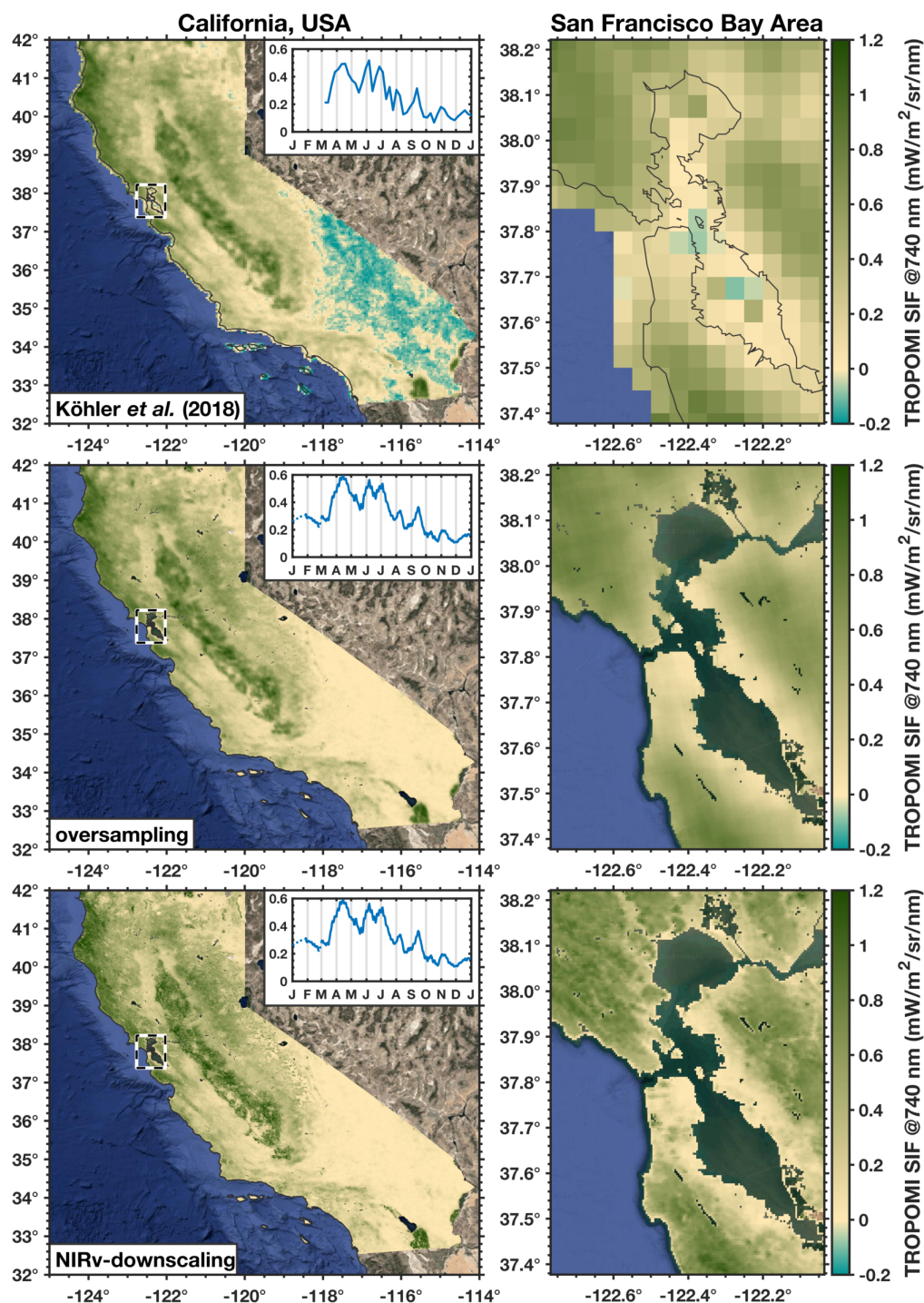


Figure 4. 2018 annual mean photosynthesis. Top row shows the 2018 annual mean TROPOMI SIF from Köhler et al. (2018) and inset shows the seasonal cycle ($0.05^\circ \times 0.05^\circ$ spatial resolution and weekly temporal resolution, respectively). Middle row uses the same TROPOMI SIF data but but oversampled to 500-m spatial resolution and daily temporal resolution. Bottom row uses an NIR_v-weighted local downscaling to 500-m spatial resolution. Left column shows all of California, USA and right column shows the San Francisco Bay Area in detail. Dashed black line in the left column indicates the domain of the right column.



1 oversampling and downscaling methods both yield consistent large-scale patterns and seasonal cycles (left panels in Fig. 4).
2 The main impact of the MODIS-based local downscaling is a sharpening effect. This can be seen in the right column of Fig. 4.
3 Importantly, the gradients observed in the oversampled SIF are also present in the downscaled SIF. The choice of MODIS
4 vegetation index to use in the downscaling makes little difference as the r^2 between the different downscaled SIF products
5 range from 0.99-1.00 (see Fig. S2), hereafter we use SIF downscaled with NIR_v because, of the three vegetation indices, NIR_v
6 showed the strongest correlation to SIF (see Fig. 2). Again, we stress that the large-scale spatio-temporal patterns are conserved
7 between the oversampling and downscaling methods and the nuanced difference in processing allow for analysis at much finer
8 spatio-temporal scales. That is to say that we are not inducing large-scale changes in the spatio-temporal patterns with these
9 different methods of processing, those are robustly driven by the underlying SIF retrievals.

10 4 Inferring GPP from SIF

11 Previous work has shown strong empirical relationships between SIF and GPP at coarse spatial scales (e.g., Walther et al.,
12 2016; Jeong et al., 2017; Parazoo et al., 2018; Zuromski et al., 2018; Sun et al., 2018b). Magney et al. (2019a) recently
13 extended this SIF-GPP relationship by showing, in a conifer forest, how both SIF and GPP are regulated by seasonal changes
14 in photoprotective pigments and how SIF is directly related to needle physiology.

15 Lee et al. (2013), Guanter et al. (2014), and Sun et al. (2017) have previously argued for a linear relationship between SIF
16 and GPP, this follows from a simple relational analysis. From Monteith theory (Monteith, 1972) we can write:

$$17 \text{ GPP} = \Phi_{\text{CO}_2} \alpha I \quad (6)$$

18 where Φ_{CO_2} is the light use efficiency of CO_2 assimilation, I is the photosynthetically active radiation (PAR), and α is the
19 fractional absorbance of PAR. An analogous expression can be written for SIF (Lee et al., 2013):

$$20 \text{ SIF} = \Phi_F \alpha \beta I \quad (7)$$

21 where Φ_F is the the light-use efficiency of SIF and β is the probability of SIF photons escaping the canopy. Rearranging yields:
22

$$23 \text{ GPP} = \frac{\Phi_{\text{CO}_2}}{\beta \Phi_F} \text{SIF}. \quad (8)$$

24 From Eq. 8 we can see that GPP should be proportional to SIF. However, there are likely differences in $\Phi_{\text{CO}_2}/(\beta \Phi_F)$ between
25 ecosystems. Notably, Yang et al. (2018) argued that SIF is more strongly correlated with the absorbed PAR (αI) than with GPP
26 at sub-daily timescales, which implicitly points to non-linearities in $\Phi_{\text{CO}_2}/(\beta \Phi_F)$. β will be a function of the canopy structure
27 and likely differs between ecosystems, although some studies have argued that reflectance measurements could be used to infer
28 β (Yang and van der Tol, 2018; Zeng et al., 2019). Additionally, the ratio of Φ_{CO_2} to Φ_F will likely be ecosystem specific
29 due to, for example, differences in photosynthetic pathways (C3 versus C4 plants; Liu et al., 2017). A number of studies have
30 found the relationship between chlorophyll fluorescence and GPP to be non-linear at the leaf-scale (e.g., Magney et al., 2017,



- 1 2019b), owing the increased linearity at the canopy scale to averaging SIF and GPP over many different leaf angles exposed to
- 2 highly heterogenous light environments.

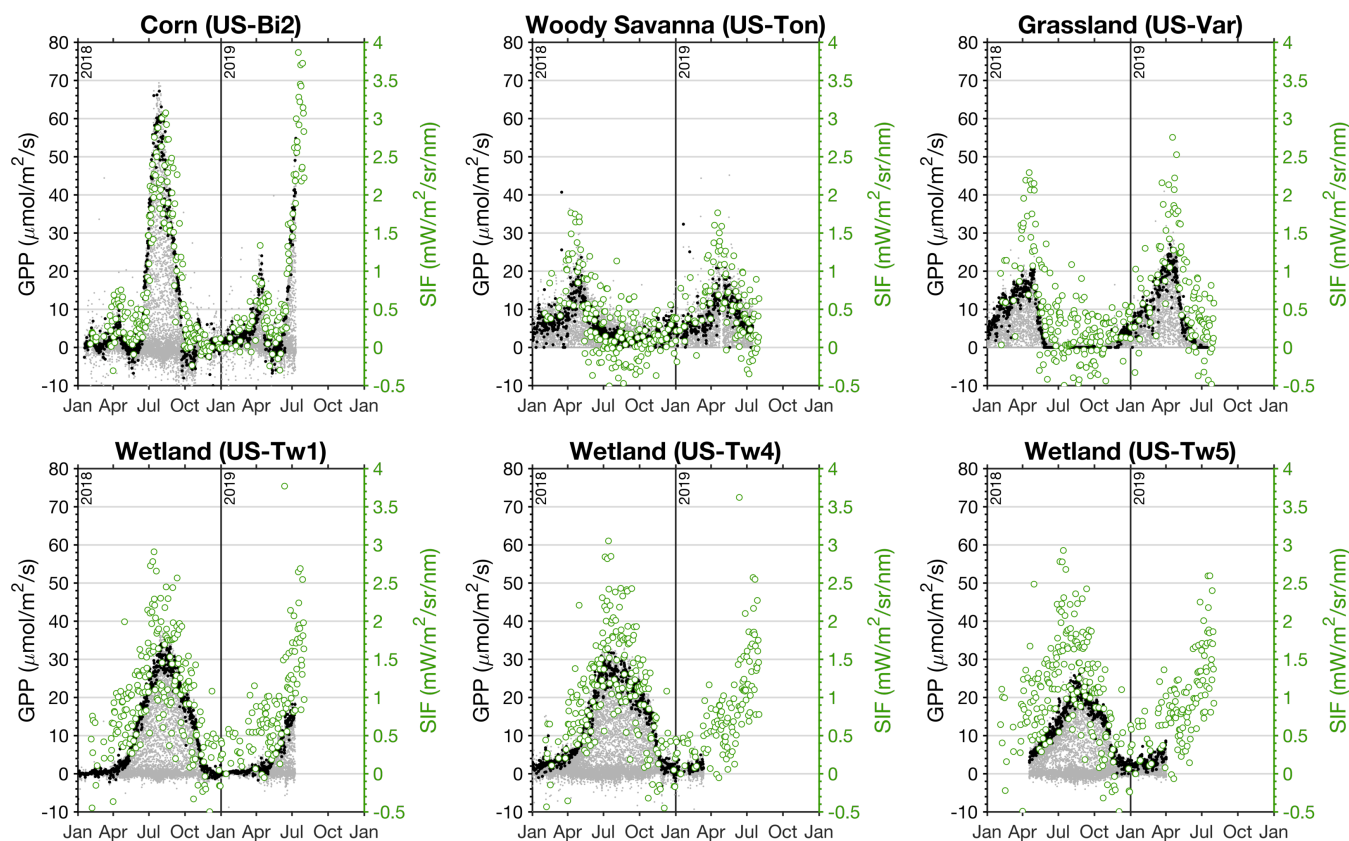


Figure 5. AmeriFlux GPP and TROPOMI SIF at six sites in California. Left axes (black) show GPP from AmeriFlux and right axes (green) show SIF from TROPOMI that have been downscaled with NIR_v . Light gray dots show all of the GPP measurements from the AmeriFlux site and black dots indicate GPP measurements between 13:00-14:00 PST (TROPOMI equatorial overpass is 13:30 local solar time). Green circles show the TROPOMI SIF observations at the AmeriFlux sites after applying the scene-specific relative weighting from the MODIS NIR_v . AmeriFlux sites used are: Bouldin Island (US-Bi2; 38.1090°N, 121.5350°W), Tonzi Ranch (US-Ton; 38.4316°N, 120.9660°W), Vaira Ranch (US-Var; 38.4133°N, 120.9507°W), Twitchell Island West Pond (US-Tw1; 38.1074°N, 121.6469°W), Twitchell Island East End (US-Tw4; 38.1030°N, 121.6414°W), and Twitchell Island East Pond (US-Twt; 38.1072°N, 121.6426°W). CO_2 flux measurements and comparisons for other sites listed in Table 1 are shown in Supplemental Figs. S3 and S4.

- 3 Figure 5 compares the TROPOMI SIF retrievals to observations from AmeriFlux sites across California (see Table 1 and
- 4 Fig. 1 for the locations). The gray dots in Fig. 5 are all of the AmeriFlux GPP estimates and the black dots are those between
- 5 13:00-14:00 PST, similar to the TROPOMI overpass time (equatorial overpass time is 13:30 local solar time at nadir). This
- 6 overpass time is fortuitous in that it generally coincides with the daily maximum in GPP at the AmeriFlux sites. The green
- 7 dots are the actual TROPOMI SIF retrievals at that location that have the scene-specific relative weighting from the MODIS



1 NIR_v (Eq. 5). No temporal smoothing has been applied in Fig. 5. We find a strong correspondence between SIF and GPP
2 across four different ecosystems. The top left panel shows that SIF clearly captures the onset of photosynthesis as well as the
3 punctuated seasonal cycle of GPP in a corn field (US-Bi2) with $r^2 = 0.79$. We also observe the gradual increase in GPP and
4 abrupt decline at a woody savanna site (US-Ton) and grassland site (US-Var) with $r^2 = 0.40$ and $r^2 = 0.59$, respectively. The
5 relatively high variability in SIF at US-Ton and US-Var from July to December ($1-\sigma$ spread of $0.33 \text{ mW/m}^2/\text{sr/nm}$) contrasts
6 the low variability during the dormant period at US-Bi2 and is likely associated with bright surfaces (implying a higher retrieval
7 uncertainty), quantifying the upper range of anticipatable noise. The bottom row of Fig. 5 shows a comparison of TROPOMI
8 SIF with GPP from three different wetland sites on Twitchell Island in the Sacramento-San Joaquin River Delta, we generally
9 find a strong correspondence between TROPOMI SIF and the three wetland sites ($r^2 = 0.42, 0.48, \text{ and } 0.29$ for US-Tw1,
10 US-Tw4, and US-Tw5). The inter-site differences in GPP within a single ecosystem are larger than the SIF-GPP differences,
11 indicating some fine-scale heterogeneity that is likely not being captured here. In any case, the reasonable agreement with the
12 GPP at the wetland sites is encouraging because standing water can often bias reflectance-based indices, particularly in the
13 NIR (Gamon et al., 2013).

14 From this SIF-GPP comparison in Fig. 5, we infer a SIF-GPP scaling factor of $18.5 \pm 4.9 [(\mu\text{mol/m}^2/\text{s})/(\text{mW/m}^2/\text{sr/nm})]$
15 across the six sites in Fig. 5 (range of scaling factors is 13-25, see Fig. S3). Our comparison of TROPOMI SIF with GPP from
16 AmeriFlux sites in California indicates larger inter-ecosystem differences in the SIF-GPP relationship than intra-ecosystem
17 differences, lending credence to this universal scaling factor. However, there are two important caveats: 1) we do not have an
18 eddy covariance site in an evergreen forest, which is a major limitation as much of California is dominated by evergreen forests
19 and 2) we are not directly measuring GPP with SIF. As such, we refer to this SIF-estimated GPP as:

$$20 \text{ GPP}^* := 18.5 \cdot \text{SIF.} \quad (9)$$

21 This single scaling from Eq. 9 seems to be a reasonable relation given the available information, with the caveat that there
22 could be differences between ecosystems that are unaccounted for.

23 5 Timing and spatial patterns of photosynthesis in California

24 Figure 6a shows the SIF-derived seasonal cycle of photosynthesis in California. One of the most prominent features is the
25 apparent double peak in the seasonal cycle. This double peak is present in both 2018 and 2019 with similar timing of the
26 maxima. The first peak occurs in April and the second peak occurs in June. Interestingly, the trough between the these peaks
27 occurs near the annual maximum in PAR (red line in Fig. 6d). This begs the question: “*What is driving this double peak in the*
28 *seasonality of California’s photosynthesis?*”

29 We can use the CropScape database (see Fig. 1) to determine the ecosystems driving the spatio-temporal patterns in the
30 TROPOMI SIF data as it provides land cover classifications across the state of California at 30-m spatial resolution. However,
31 a notable limitation of the classifications from the CropScape data is the lack of discrimination for non-cropland areas. For
32 example, grasslands and pastures are combined into a single land type that seems to also include regions that would typically

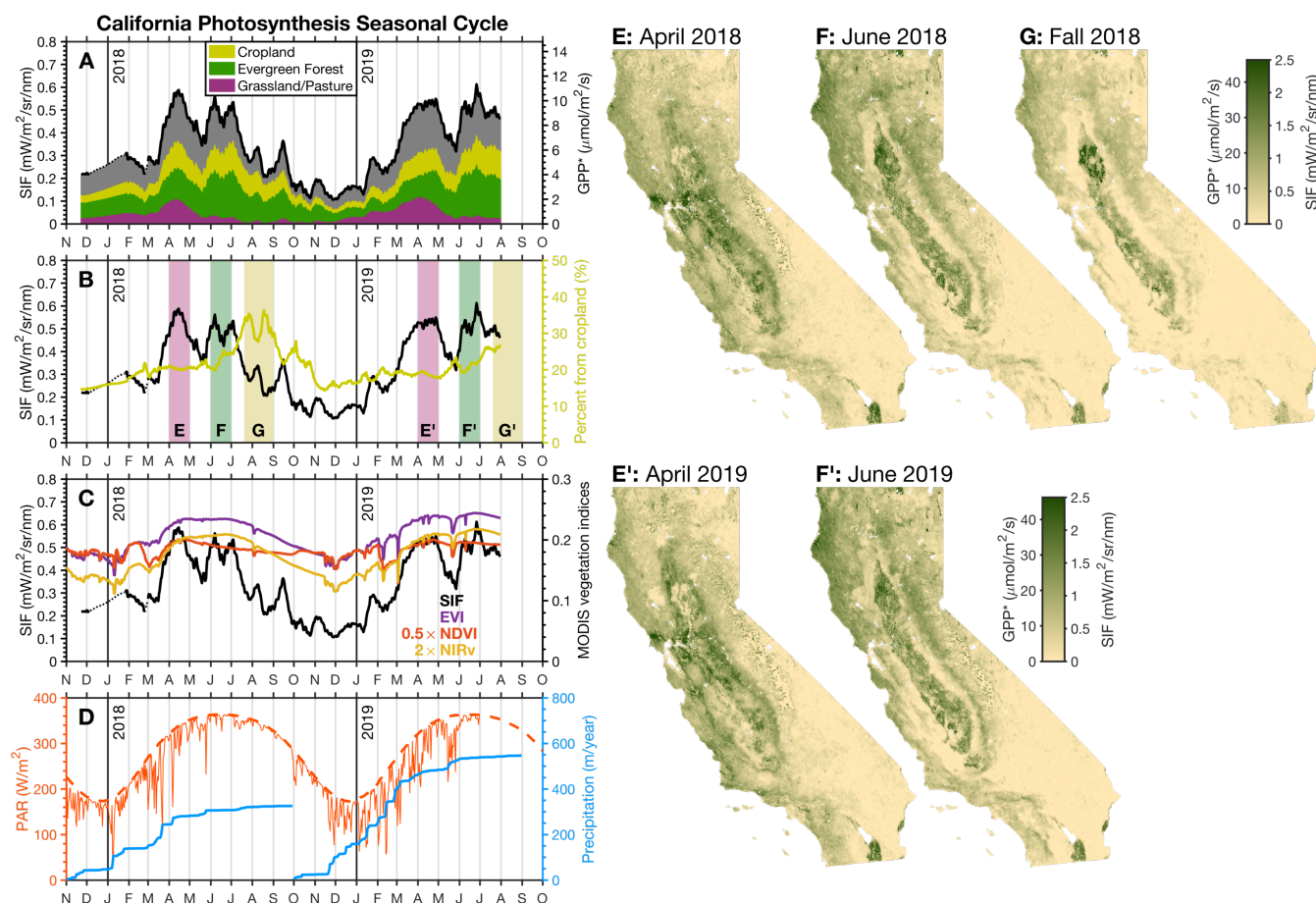


Figure 6. Seasonal cycle of photosynthesis in California. Panel A shows the statewide mean SIF (black line) at 13:30 PST from November 2017 through September 2019 broken down by the contributions coming from cropland (yellow), evergreen forests (green), grasslands or pastures (purple), and other (gray). Rice is included in cropland here. Land types are taken from the 2018 CropScape database shown in Figure 1. Right axis shows the estimated GPP* based on comparison with AmeriFlux sites in California. Panel B shows the percentage of SIF coming from cropland (yellow). Vertical bars indicate the time periods with corresponding spatial plots in Panels E–G'. Panel C shows the vegetation indices (NDVI, EVI, and NIR_v) from MODIS over the same time period. Panel D shows clear sky PAR over California at 13:00 PST (dashed red line), surface PAR estimated from the ERA-Interim Reanalysis (thin red line), and cumulative precipitation over the water year from the GPM satellite (blue). Panels E–G' show the spatial patterns of SIF for the time periods indicated in Panel B.

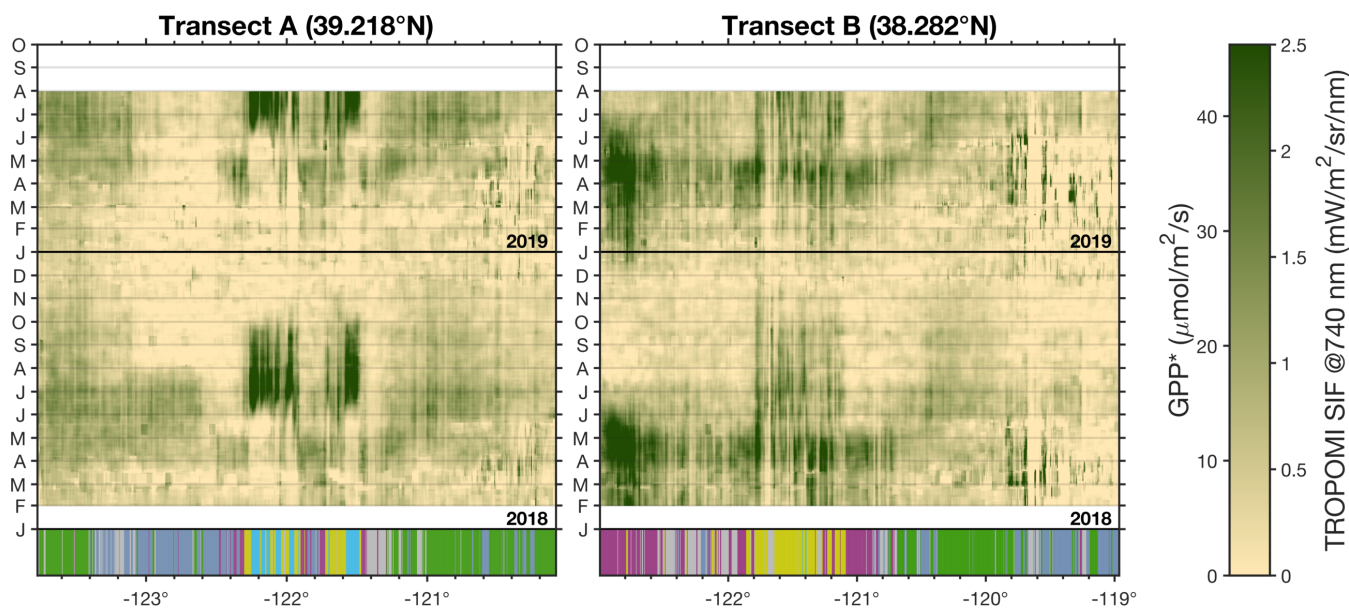


Figure 7. Hovmöller diagrams for three transects across California. Panels show Hovmöller diagrams from November 2017 through March 2019 for the two transects shown in Fig. 1. Bottom bar indicates the dominant land type with coloring from Fig. 1: green is evergreen forest, purple is grassland/pasture, cyan is rice, yellow is cropland (excluding rice), blue is shrubland, and gray is other.

1 be defined as oak savanna and chaparral. In lieu of a better sub-kilometer land cover dataset, we use the classifications from
2 the CropScape database for this work.

3 Figure 6a shows a breakdown of the regions contributing to the statewide SIF signal based on the land cover data from
4 the CropScape database. We find the California grasslands and pastures (a single classification that also includes chaparral
5 and oak savanna) have a single peak that coincides with the first statewide peak in April, this is consistent with the seasonal
6 cycle at California grassland sites in the AmeriFlux network (Fig. 5) that show a unimodal peak in the spring that ends in
7 May. Figs. 6e and 6e' show the mean spatial pattern in April 2018 and 2019, respectively, where we see that the April peak
8 coincides with a statewide increase in SIF. There are a few pertinent hotspots in grasslands or pastures during this April peak.
9 Notably, California's Central Valley and surrounding hills exhibit a strong photosynthesis signal in April. The valley to the east
10 of Bodega Bay (38.3°N, 122.9°W) appears as a large hotspot in both 2018 and 2019. This region lies on Transect B in Fig. 1
11 and the seasonal cycle is shown in more detail in Fig. 7.

12 The second peak in June shows a dominant contribution from evergreen forests (Fig. 6a). This can also be seen in the
13 spatial patterns from Fig. 6f and 6f' where the evergreen forests in Northern California exhibit a strong SIF signal. California's
14 Central Valley can be clearly distinguished as the surrounding hills have dried out (predominantly oak savanna and chaparral).
15 The observed photosynthesis from the Central Valley is maintained by heavily irrigated cropland throughout the valley.

16 The yellow line in Fig. 6b indicates the fraction of SIF in California that comes from cropland. We see the largest relative
17 contribution occurring in the fall. However, this is primarily because all other ecosystems have gone dormant (see Fig. 6g)



- 1 as opposed to an increase in photosynthetic activity from cropland. The only region that shows an increase in photosynthesis
- 2 are the rice fields in the Sacramento Valley (the valley surrounding Sutter Buttes at 39.1°N, 121.5°W) in Northern California.
- 3 The rice fields show a SIF signal in excess of 2.5 mW/m²/sr/nm during the fall (GPP* in excess of 45 μmol/m²/s).

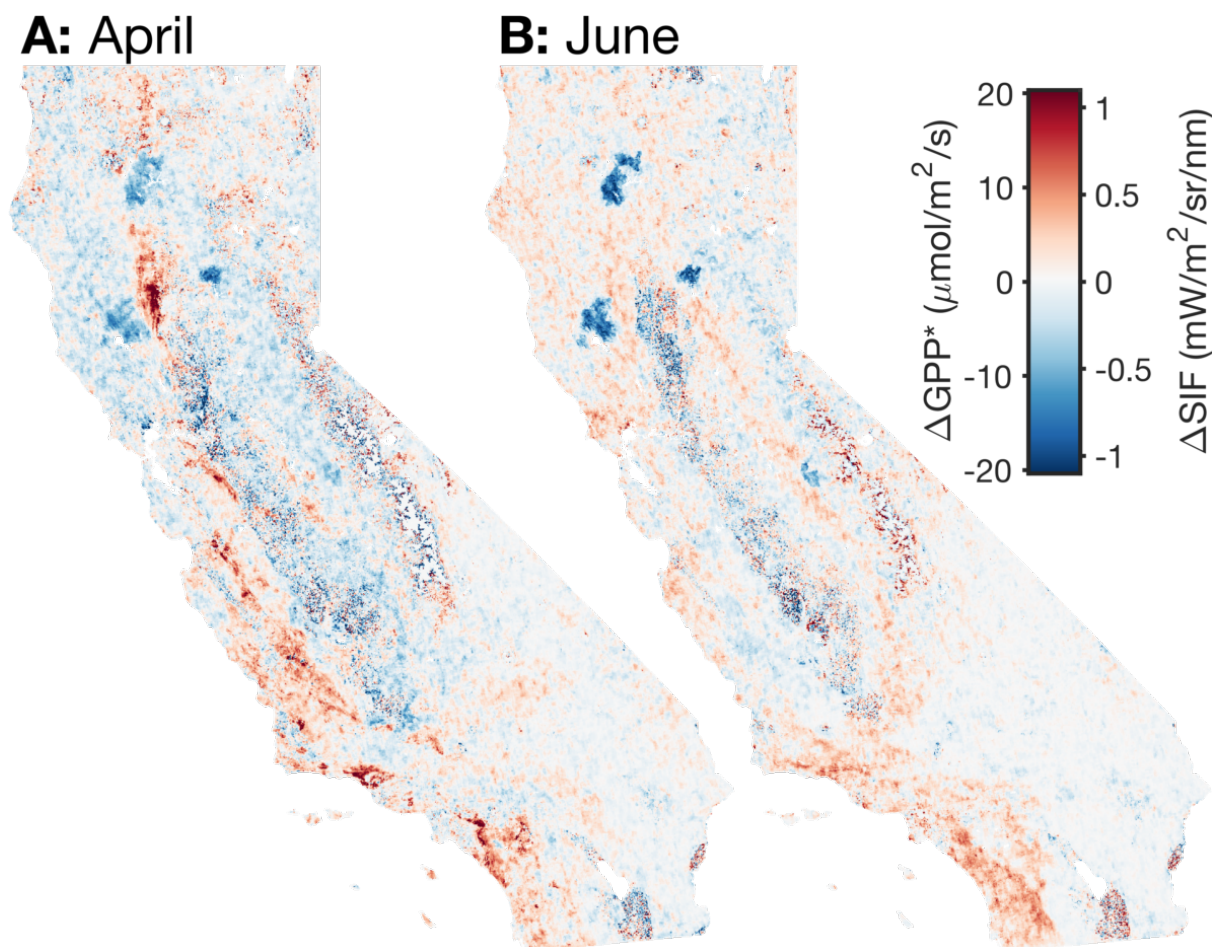


Figure 8. Difference between 2019 and 2018. Panel A shows the difference between the mean SIF in April 2019 and 2018. **Panel B** and **Panel C** are the same as panel A but for June and Fall (July 20-August 31), respectively. Red indicates higher SIF in 2019, blue indicates higher SIF in 2018.

- 4 Both 2018 and 2019 show a double peak in the seasonal cycle, however, the onset of the grassland driven peak differs
- 5 substantially between the two years. This difference is likely driven by the increased precipitation in 2019 (blue line in Fig. 6d).
- 6 There was 50% more precipitation in 2019 compared to 2018 and the precipitation occurred earlier in the water year. By mid-
- 7 February 2019 there was more precipitation than the annual total from 2018. This early precipitation allowed for an earlier and
- 8 longer growing season for the grasses. Figure 8 shows the difference in spatial patterns between 2019 and 2018. In general, we
- 9 find reasonable consistency between the two years. Most of the major differences are due to ecosystem disturbances such as



1 fires. The 2018 Northern California fires are a striking example of that (three large negative anomalies in Fig. 8b), the impact
2 of these fires is currently the focus of forthcoming work. An additional feature that stands out is the positive SIF anomaly in
3 Southern California, this increase in 2019 is due to the low rainfall the previous year.

4 Interestingly, none of the MODIS vegetation indices (NDVI, EVI, or NIR_v) show this double peak in photosynthesis
5 (Fig. 6c). The seasonal cycles from the three vegetation indices show a greening that starts in mid-winter (begins in De-
6 cember 2018) and increases roughly linearly to a peak in April. All three vegetation indices maintain that peak until July when
7 they show a roughly linear decline through the Fall. The seasonal cycle of the three MODIS vegetation indices bear a strong
8 similarity to the clear sky PAR seasonal cycle. This difference between SIF and the MODIS vegetation indices may be due to a
9 clear sky bias as the reflectance-based vegetation indices (NDVI, EVI, and NIR_v) can only be made under clear sky conditions,
10 whereas SIF can be retrieved in the presence of some clouds and aerosols (Frankenberg et al., 2011b). This is inferred by the
11 decline in PAR during May 2018 and May 2019 (Fig. 6d) that corresponds with a decline in SIF. This highlights one of the
12 differences between SIF and the MODIS vegetation indices, the vegetation indices are reflectance-based products whereas SIF
13 is a fluorescence signal emitted during photosynthesis and is thus coupled to the radiation regime. This again gets back to the
14 idea that SIF is measuring photosynthetic activity whereas the MODIS indices are measuring photosynthetic capacity.

15 Several ecophysiological reasons could also explain the SIF detection of a double peak feature, whereas MODIS vegetation
16 indices do not. Nearly 11% of the state of California consists of the California oak savanna (many in the foothills of coastal
17 mountains and the Sierras; Tyler et al., 2006). Over the course of the season, these ecosystems operate as an evergreen ecosys-
18 tem, whereby understory grass is photosynthetically active during the winter months, while trees (primarily oak species) reach
19 extremely high values of maximum carboxylation capacity (V_{cmax}) during the spring when water is plentiful, and then retain
20 their leaves throughout the summer in a highly photoprotective state (i.e., US-Ton; Xu and Baldocchi, 2003). Spatially, we
21 observe increased SIF values in oak savanna as well as chaparral ecosystems (also present on coastal and Sierra foothills) in
22 the early spring when available soil moisture is at a maximum (Xu and Baldocchi, 2004; Xu et al., 2004). As these ecosystems
23 enter the hot, dry summers, increases in sustained non-photochemical quenching and decreases in photochemistry result in
24 decreased fluorescence, while still appearing “green” to MODIS vegetation indices. Meanwhile, snow is melting rapidly at
25 higher elevations, making water available for many of the needleleaf evergreen species in the Sierras and Coastal ranges, then
26 the water resources become depleted and temperatures cool prompting these evergreen species to go back into a photoprotec-
27 tive state, resulting in a short photosynthetically active growing season that has been shown to be more well characterized by
28 SIF from GOME-2 than MODIS NDVI and EVI (Zuromski et al., 2018).

29 Figure 7 shows a Hovmöller diagram for three transects across Northern California (see Figure 1 for the location of the
30 transects). Transect A in Figure 7 shows the short but strong SIF signal from the rice fields. The timing of the SIF signal
31 from the rice fields agrees with the growing cycle for rice in California. Rice in the Sacramento Valley is typically planted in
32 mid-to-late May, the fields are then flooded, and harvested in mid-to-late September (University of California at Davis, 2018).
33 This observation of the rice fields is encouraging because we are observing photosynthesis in the presence of standing water,
34 which can often bias reflectance-based indices in the NIR (Gamon et al., 2013). In both 2018 and 2019 we observe the onset
35 of photosynthesis at the rice fields in the first few days of June and a rapid decline at the end of September. Transect B begins



1 in the valley to the east of Bodega Bay (location of the grassland hotspot) and crosses the central valley. This grassland hotspot
2 is present from April through May of both 2018 and 2019. The valley near Bodega Bay is dominated by pastures, however it
3 is currently unclear why this particular region exhibits a stronger SIF signal than other pastures in California. The persistent
4 strong signal in 2018 and 2019 might make it an interesting site for study with an eddy covariance site in the future.

5 6 Dominant “modes” of variability in California’s photosynthesis

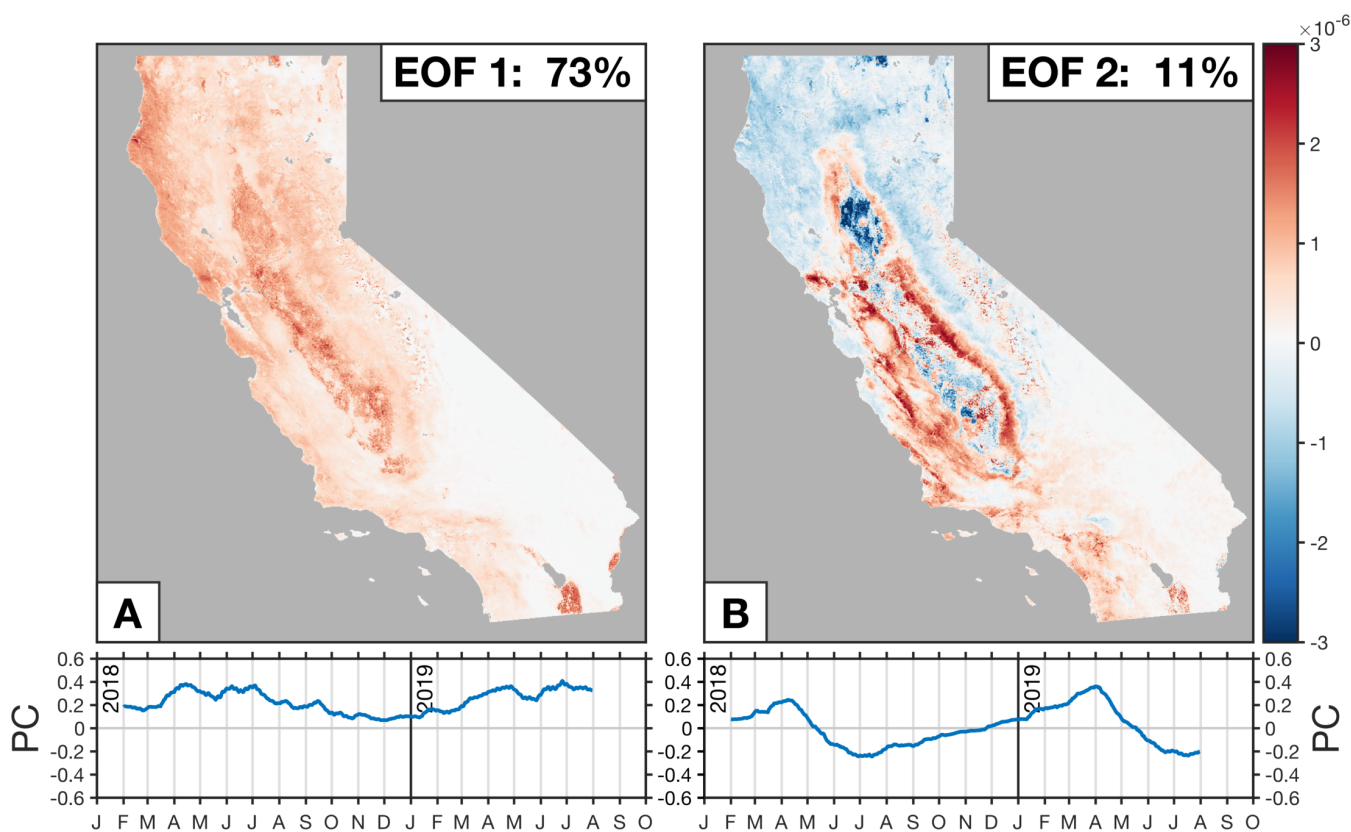


Figure 9. EOFs and PCs for TROPOMI SIF over California. Panels show the first two EOFs and PCs. EOFs are unit length (sum of the squares is equal to 1) and computed using unnormalized SIF spatially downscaled with NIR_v . Time series show the corresponding PC (blue line) from February 2018 through September 2019. Length of the PC is equal to the corresponding eigenvalue and has units of $mW/m^2/sr/nm$. Text in figure lists the percent of variance explained by that EOF. Fig. S5 shows the corresponding eigenvalue spectrum for the TROPOMI SIF data over California.

6 Section 5 discussed the spatio-temporal patterns for different regions and ecosystems, here we present an alternative method
7 of characterizing the dominant modes of spatio-temporal variability in photosynthesis using Empirical Orthogonal Functions
8 (EOFs) and their associated Principal Components (PCs). EOFs are a matrix factorization that are commonly used to identify



1 structure in a spatial dataset and yield a finite number of modes. These modes compactly represent the data and are often
2 interpreted as physical modes of the system.

3 Figure 9 shows the first two EOFs and their associated PCs for the TROPOMI SIF data over California, the corresponding
4 eigenvalue spectrum can be seen in Fig. S5. The first two EOFs corroborate the findings from Section 5 and, taken together,
5 explain 84% of the variability in the TROPOMI SIF data:

- 6 – EOF 1: the mean signal
- 7 – EOF 2: the double peak

8 The first EOF (Fig. 9a) represents the mean signal and explains 73% of the variability in the TROPOMI SIF data. From the
9 spatial pattern we can see that it includes most of the biomass in California and is strongly correlated to the state-wide mean
10 SIF: $r^2 = 0.99$. The associated principal component bears a strong similarity to the statewide mean SIF seasonal cycle (Fig. 6a).
11 This finding is not entirely surprising because we are using un-normalized SIF data for the matrix factorization. This means
12 that the most important mode of variability is the mean signal and that the following EOFs are anomalies relative to the mean
13 signal.

14 The second EOF (Fig. 9b) represents the double peak in the timing of California's photosynthesis. This EOF combines the
15 signal from the grasslands (positive phase of EOF 2) and the evergreen forests (negative phase of EOF 2). We find EOF 2
16 to be positively correlated with the grassland fraction from the CropScape database ($r = 0.55$) and negatively correlated with
17 the evergreen forests ($r = -0.37$). There is also a negative correlation with the rice fields ($r = -0.31$). The associated principle
18 component serves to amplify the seasonal cycle from EOF 1 in grasslands during April and amplify the forest peak in June.
19 This is because the red region (grasslands) in Fig. 9b will contribute a positive anomaly in April and a negative anomaly in June.
20 Conversely, the blue region (evergreen forests and rice) will contribute a negative anomaly in April and a positive anomaly in
21 June. This EOF arises because the grasslands and forests are both spatially separated and out of phase with each other, allowing
22 the matrix factorization to place them into a single EOF that represents the processes driving the double peak in the timing of
23 California's photosynthesis.

24 It should be noted that these EOF patterns found here are unlikely to be true "physical modes" (see, for example, Monahan
25 et al., 2009). That is to say, we would not necessarily expect the response to a perturbation to follow patterns shown in Fig. 9.
26 EOF 2 is a good example of this because it seems unlikely that the grasslands and forests will exhibit opposing responses to a
27 forcing. Grasslands and forests are combined into a single EOF simply because there is little loss of information by combining
28 them due to the spatial separation and phase offset. This is not to argue against the utility of EOFs. EOFs are a useful method
29 for identifying structure in geophysical datasets, as evidenced here by their identification of the double peak in the timing of
30 California's photosynthesis.



1 7 Conclusions

2 We present an oversampling and downscaling method to obtain daily estimates of Solar Induced chlorophyll Fluorescence
3 (SIF), a proxy for photosynthetic activity, at 500-m spatial resolution from TROPOMI. To our knowledge, this is the highest
4 spatial resolution SIF dataset from satellite measurements. We find a double peak in the seasonality of photosynthesis in
5 California during 2018 and 2019, a feature that is not present in the MODIS vegetation indices (NDVI, EVI, or NIR_v). Analysis
6 of the spatial and temporal patterns of the SIF data indicates that the double peak is due to two processes that are out of phase
7 with each other: woody grasslands (e.g., grasslands, chaparral, and oak savanna) and evergreen forests.

8 Our work applies methods developed for previous satellite retrievals (oversampling) and uses estimates of sub-grid scale
9 vegetation (downscaling) to obtain daily 500-m spatial resolution SIF from TROPOMI over California. The oversampling
10 method results in a smooth spatial field and removes artifacts due to complex topography and the wide TROPOMI swath. The
11 downscaling method further refines the high resolution spatial patterns by bringing in *a priori* information on the sub-grid
12 vegetation patterns. The oversampling and downscaling methods do not alter the large scale spatio-temporal patterns as they
13 conserve the SIF signal over a single scene.

14 TROPOMI SIF data and MODIS vegetation indices are reasonably consistent at annual timescales over California, but show
15 weaker relationships at daily and monthly timescales. This implies that TROPOMI SIF is providing some information that is
16 distinct from the MODIS vegetation indices. TROPOMI SIF data show a strong correspondence with half-hourly estimates of
17 GPP at multiple AmeriFlux sites across different ecosystems including: cropland, grassland, savanna, and wetlands. We find a
18 linear relationship between SIF and GPP that is largely invariant across ecosystems with an intercept that is not significantly
19 different from zero. As such, we use SIF as an estimate of GPP* with the caveat that some ecosystems are not represented in
20 our California analysis.

21 TROPOMI SIF data show a double peak in the seasonality of photosynthesis in California, a feature that is not present in the
22 MODIS vegetation indices. The double peak in the seasonality of California's photosynthesis is due to two processes that are
23 out of phase with each other: grasses show a maximum in April and evergreen forests peak in June. An empirical orthogonal
24 function (EOF) analysis corroborates the phase offset and spatial patterns driving the double peak. The EOF analysis also
25 indicates that two spatio-temporal patterns explain 84% of the variability in the TROPOMI SIF data.

26 The results shown here are promising for obtaining global near-daily GPP at sub-kilometer spatial scales using satellite
27 measurements. This, in turn, may prove helpful in addressing long-standing questions regarding the mechanisms and locations
28 driving carbon uptake in the Northern Hemisphere. It would also allow us to monitor climate change impacts on vulnerable
29 ecosystems at local-to-global scales.

30 *Acknowledgements.* A. J. Turner is supported as a Miller Fellow with the Miller Institute for Basic Research in Science at UC Berkeley.
31 R. C. Cohen acknowledges support from the TEMPO project SV3-83019. P. Köhler and C. Frankenberg are funded by the Earth Science
32 U.S. participating investigator (grant: NNX15AH95G). This research used the Savio computational cluster resource provided by the Berke-
33 ley Research Computing program at the University of California, Berkeley (supported by the UC Berkeley Chancellor, Vice Chancellor for



1 Research, and Chief Information Officer). This research also used resources from the National Energy Research Scientific Computing Center,
2 which is supported by the Office of Science of the U.S. Department of Energy under Contract No. DE-AC02-05CH11231. TROPOMI SIF and
3 MODIS NBAR data are publicly available at “<ftp://fluo.gps.caltech.edu/data/tropomi/>” and “<https://e4ftl01.cr.usgs.gov/MOTA/MCD43A4.006/>”,
4 respectively. Funding for AmeriFlux data resources was provided by the U.S. Department of Energy’s Office of Science. We would like to
5 thank Dennis Baldocchi (UC Berkeley) for sharing the AmeriFlux data and for providing extensive feedback on the work. Finally, we are
6 extremely grateful to the team that has realized the TROPOMI instrument, consisting of the partnership between Airbus Defence and Space,
7 KNMI, SRON, and TNO, commissioned by NSO and ESA.



1 References

- 2 Anav, A., Friedlingstein, P., Beer, C., Ciais, P., Harper, A., Jones, C., Murray-Tortarolo, G., Papale, D., Parazoo, N. C., Peylin, P., Piao, S.,
3 Sitch, S., Viovy, N., Wiltshire, A., and Zhao, M.: Spatiotemporal patterns of terrestrial gross primary production: A review, *Rev Geophys*,
4 53, 785–818, <https://doi.org/10.1002/2015rg000483>, 2015.
- 5 Badgley, G., Field, C. B., and Berry, J. A.: Canopy near-infrared reflectance and terrestrial photosynthesis, *Sci Adv*, 3, e1602244,
6 <https://doi.org/10.1126/sciadv.1602244>, 2017.
- 7 Badgley, G., Anderegg, L. D. L., Berry, J. A., and Field, C. B.: Terrestrial Gross Primary Production: Using NIR_V to Scale from Site to
8 Globe, *Global change biology*, <https://doi.org/10.1111/gcb.14729>, 2019.
- 9 Baker, N. R.: Chlorophyll fluorescence: a probe of photosynthesis in vivo, *Annual review of plant biology*, 59, 89–113,
10 <https://doi.org/10.1146/annurev.arplant.59.032607.092759>, 2008.
- 11 Baldocchi, D., Falge, E., Gu, L., Olson, R., Hollinger, D., Running, S., Anthoni, P., Bernhofer, C., Davis, K., Evans, R., Fuentes, J., Gold-
12 stein, A., Katul, G., Law, B., Lee, X., Malhi, Y., Meyers, T., Munger, W., Oechel, W., Paw, K. T., Pilegaard, K., Schmid, H. P., Valen-
13 tini, R., Verma, S., Vesala, T., Wilson, K., and Wofsy, S.: FLUXNET: A New Tool to Study the Temporal and Spatial Variability of
14 Ecosystem–Scale Carbon Dioxide, Water Vapor, and Energy Flux Densities, *Bulletin of the American Meteorological Society*, 82, 2415–
15 2434, [https://doi.org/10.1175/1520-0477\(2001\)082<2415:fantts>2.3.co;2](https://doi.org/10.1175/1520-0477(2001)082<2415:fantts>2.3.co;2), 2001.
- 16 Baldocchi, D. D., Hicks, B. B., and Meyers, T. P.: Measuring Biosphere–Atmosphere Exchanges of Biologically Related Gases with Microm-
17 eteorological Methods, *Ecology*, 69, 1331–1340, <https://doi.org/10.2307/1941631>, 1988.
- 18 Ballantyne, A. P., Alden, C. B., Miller, J. B., Tans, P. P., and White, J. W.: Increase in observed net carbon dioxide uptake by land and oceans
19 during the past 50 years, *Nature*, 488, 70–2, <https://doi.org/10.1038/nature11299>, 2012.
- 20 Ciais, P., Tan, J., Wang, X., Roedenbeck, C., Chevallier, F., Piao, S. L., Moriarty, R., Broquet, G., Le Quere, C., Canadell, J. G., Peng, S.,
21 Poulter, B., Liu, Z., and Tans, P.: Five decades of northern land carbon uptake revealed by the interhemispheric CO₂ gradient, *Nature*, 568,
22 221–225, <https://doi.org/10.1038/s41586-019-1078-6>, 2019.
- 23 Drusch, M., Moreno, J., Del Bello, U., Franco, R., Goulas, Y., Huth, A., Kraft, S., Middleton, E. M., Miglietta, F., Mohammed, G., Ned-
24 bal, L., Rascher, U., Schuttemeyer, D., and Verhoef, W.: The FLuorescence EXplorer Mission Concept–ESA’s Earth Explorer 8, *IEEE*
25 *Transactions on Geoscience and Remote Sensing*, 55, 1273–1284, <https://doi.org/10.1109/tgrs.2016.2621820>, 2017.
- 26 Frankenberg, C., Butz, A., and Toon, G. C.: Disentangling chlorophyll fluorescence from atmospheric scattering effects in O₂A-band spectra
27 of reflected sun-light, *Geophysical Research Letters*, 38, <https://doi.org/10.1029/2010gl045896>, 2011a.
- 28 Frankenberg, C., Fisher, J. B., Worden, J., Badgley, G., Saatchi, S. S., Lee, J.-E., Toon, G. C., Butz, A., Jung, M., Kuze, A., and Yokota,
29 T.: New global observations of the terrestrial carbon cycle from GOSAT: Patterns of plant fluorescence with gross primary productivity,
30 *Geophys Res Lett*, 38, <https://doi.org/10.1029/2011gl048738>, 2011b.
- 31 Frankenberg, C., O’Dell, C., Guanter, L., and McDuffie, J.: Remote sensing of near-infrared chlorophyll fluorescence from space in scattering
32 atmospheres: implications for its retrieval and interferences with atmospheric CO₂ retrievals, *Atmospheric Measurement Techniques*, 5,
33 2081–2094, <https://doi.org/10.5194/amt-5-2081-2012>, 2012.
- 34 Frankenberg, C., O’Dell, C., Berry, J., Guanter, L., Joiner, J., Köhler, P., Pollock, R., and Taylor, T. E.: Prospects for chloro-
35 phyll fluorescence remote sensing from the Orbiting Carbon Observatory-2, *Remote Sensing of Environment*, 147, 1–12,
36 <https://doi.org/10.1016/j.rse.2014.02.007>, 2014.



- 1 Gamon, J. A., Huemmrich, K. F., Stone, R. S., and Tweedie, C. E.: Spatial and temporal variation in primary productivity (NDVI) of
2 coastal Alaskan tundra: Decreased vegetation growth following earlier snowmelt, *Remote Sensing of Environment*, 129, 144–153,
3 <https://doi.org/10.1016/j.rse.2012.10.030>, 2013.
- 4 Guanter, L., Frankenberg, C., Dudhia, A., Lewis, P. E., Gomez-Dans, J., Kuze, A., Suto, H., and Grainger, R. G.: Retrieval and global
5 assessment of terrestrial chlorophyll fluorescence from GOSAT space measurements, *Remote Sensing of Environment*, 121, 236–251,
6 <https://doi.org/10.1016/j.rse.2012.02.006>, 2012.
- 7 Guanter, L., Zhang, Y., Jung, M., Joiner, J., Voigt, M., Berry, J. A., Frankenberg, C., Huete, A. R., Zarco-Tejada, P., Lee, J. E., Moran,
8 M. S., Ponce-Campos, G., Beer, C., Camps-Valls, G., Buchmann, N., Gianelle, D., Klumpp, K., Cescatti, A., Baker, J. M., and Griffis,
9 T. J.: Global and time-resolved monitoring of crop photosynthesis with chlorophyll fluorescence, *Proceedings of the National Academy*
10 *of Sciences of the United States of America*, 111, E1327–33, <https://doi.org/10.1073/pnas.1320008111>, 2014.
- 11 Guanter, L., Aben, I., Tol, P., Krijger, J. M., Hollstein, A., Köhler, P., Damm, A., Joiner, J., Frankenberg, C., and Landgraf, J.: Potential
12 of the TROPospheric Monitoring Instrument (TROPOMI) onboard the Sentinel-5 Precursor for the monitoring of terrestrial chlorophyll
13 fluorescence, *Atmospheric Measurement Techniques*, 8, 1337–1352, <https://doi.org/10.5194/amt-8-1337-2015>, 2015.
- 14 Hemes, K. S., Chamberlain, S. D., Eichelmann, E., Anthony, T., Valach, A., Kasak, K., Szutu, D., Verfaillie, J., Silver, W. L., and Baldocchi,
15 D. D.: Assessing the carbon and climate benefit of restoring degraded agricultural peat soils to managed wetlands, *Agricultural and Forest*
16 *Meteorology*, 268, 202–214, <https://doi.org/10.1016/j.agrformet.2019.01.017>, 2019.
- 17 IPCC: Climate Change 2013: The Physical Science Basis. Contribution of Working Group I to the Fifth Assessment Report of the Intergov-
18 ernmental Panel on Climate Change, Tech. rep., IPCC, 2013.
- 19 Jeong, S.-J., Schimel, D., Frankenberg, C., Drewry, D. T., Fisher, J. B., Verma, M., Berry, J. A., Lee, J.-E., and Joiner, J.: Application of
20 satellite solar-induced chlorophyll fluorescence to understanding large-scale variations in vegetation phenology and function over northern
21 high latitude forests, *Remote Sensing of Environment*, 190, 178–187, <https://doi.org/10.1016/j.rse.2016.11.021>, 2017.
- 22 Joiner, J., Yoshida, Y., Vasilkov, A. P., Yoshida, Y., Corp, L. A., and Middleton, E. M.: First observations of global and seasonal terrestrial
23 chlorophyll fluorescence from space, *Biogeosciences*, 8, 637–651, <https://doi.org/10.5194/bg-8-637-2011>, 2011.
- 24 Joiner, J., Yoshida, Y., Vasilkov, A. P., Middleton, E. M., Campbell, P. K. E., Yoshida, Y., Kuze, A., and Corp, L. A.: Filling-in of near-infrared
25 solar lines by terrestrial fluorescence and other geophysical effects: simulations and space-based observations from SCIAMACHY and
26 GOSAT, *Atmospheric Measurement Techniques*, 5, 809–829, <https://doi.org/10.5194/amt-5-809-2012>, 2012.
- 27 Joiner, J., Guanter, L., Lindstrot, R., Voigt, M., Vasilkov, A. P., Middleton, E. M., Huemmrich, K. F., Yoshida, Y., and Frankenberg, C.: Global
28 monitoring of terrestrial chlorophyll fluorescence from moderate-spectral-resolution near-infrared satellite measurements: methodology,
29 simulations, and application to GOME-2, *Atmospheric Measurement Techniques*, 6, 2803–2823, [https://doi.org/10.5194/amt-6-2803-](https://doi.org/10.5194/amt-6-2803-2013)
30 2013, 2013.
- 31 Joiner, J., Yoshida, Y., Vasilkov, A. P., Schaefer, K., Jung, M., Guanter, L., Zhang, Y., Garrity, S., Middleton, E. M., Huemm-
32 rich, K. F., Gu, L., and Belelli Marchesini, L.: The seasonal cycle of satellite chlorophyll fluorescence observations and its re-
33 lationship to vegetation phenology and ecosystem atmosphere carbon exchange, *Remote Sensing of Environment*, 152, 375–391,
34 <https://doi.org/10.1016/j.rse.2014.06.022>, 2014.
- 35 Joiner, J., Yoshida, Y., Guanter, L., and Middleton, E. M.: New methods for the retrieval of chlorophyll red fluorescence from hyperspectral
36 satellite instruments: simulations and application to GOME-2 and SCIAMACHY, *Atmospheric Measurement Techniques*, 9, 3939–3967,
37 <https://doi.org/10.5194/amt-9-3939-2016>, 2016.



- 1 Köhler, P., Guanter, L., and Joiner, J.: A linear method for the retrieval of sun-induced chlorophyll fluorescence from GOME-2 and SCIA-
- 2 MACHY data, *Atmospheric Measurement Techniques*, 8, 2589–2608, <https://doi.org/10.5194/amt-8-2589-2015>, 2015.
- 3 Köhler, P., Frankenberg, C., Magney, T. S., Guanter, L., Joiner, J., and Landgraf, J.: Global Retrievals of Solar-Induced Chlorophyll Flu-
- 4 orescence With TROPOMI: First Results and Intersensor Comparison to OCO-2, *Geophysical Research Letters*, 45, 10,456–10,463,
- 5 <https://doi.org/10.1029/2018gl079031>, 2018.
- 6 Kuze, A., Suto, H., Nakajima, M., and Hamazaki, T.: Thermal and near infrared sensor for carbon observation Fourier-
- 7 transform spectrometer on the Greenhouse Gases Observing Satellite for greenhouse gases monitoring, *Appl Opt*, 48, 6716–33,
- 8 <https://doi.org/10.1364/AO.48.006716>, 2009.
- 9 Lee, J. E., Frankenberg, C., van der Tol, C., Berry, J. A., Guanter, L., Boyce, C. K., Fisher, J. B., Morrow, E., Worden, J. R., Asefi, S.,
- 10 Badgley, G., and Saatchi, S.: Forest productivity and water stress in Amazonia: observations from GOSAT chlorophyll fluorescence, *Proc.*
- 11 *Biol. Sci.*, 280, 20130 171, <https://doi.org/10.1098/rspb.2013.0171>, 2013.
- 12 Li, X. and Xiao, J.: A Global, 0.05-Degree Product of Solar-Induced Chlorophyll Fluorescence Derived from OCO-2, MODIS, and Reanal-
- 13 ysis Data, *Remote Sensing*, 11, 517, <https://doi.org/10.3390/rs11050517>, 2019.
- 14 Liu, L., Guan, L., and Liu, X.: Directly estimating diurnal changes in GPP for C3 and C4 crops using far-red sun-induced chlorophyll
- 15 fluorescence, *Agricultural and Forest Meteorology*, 232, 1–9, <https://doi.org/10.1016/j.agrformet.2016.06.014>, 2017.
- 16 Luus, K. A., Commane, R., Parazoo, N. C., Benmergui, J., Euskirchen, E. S., Frankenberg, C., Joiner, J., Lindaas, J., Miller, C. E., Oechel,
- 17 W. C., Zona, D., Wofsy, S., and Lin, J. C.: Tundra photosynthesis captured by satellite-observed solar-induced chlorophyll fluorescence,
- 18 *Geophysical Research Letters*, 44, 1564–1573, <https://doi.org/10.1002/2016gl070842>, 2017.
- 19 Magney, T. S., Frankenberg, C., Fisher, J. B., Sun, Y., North, G. B., Davis, T. S., Kornfeld, A., and Siebke, K.: Connecting active to passive
- 20 fluorescence with photosynthesis: a method for evaluating remote sensing measurements of Chl fluorescence, *The New phytologist*, 215,
- 21 1594–1608, <https://doi.org/10.1111/nph.14662>, 2017.
- 22 Magney, T. S., Bowling, D. R., Logan, B. A., Grossmann, K., Stutz, J., Blanken, P. D., Burns, S. P., Cheng, R., Garcia, M. A., Köhler,
- 23 P., Lopez, S., Parazoo, N. C., Raczka, B., Schimel, D., and Frankenberg, C.: Mechanistic evidence for tracking the seasonality of pho-
- 24 tosynthesis with solar-induced fluorescence, *Proceedings of the National Academy of Sciences of the United States of America*, 116,
- 25 11 640–11 645, <https://doi.org/10.1073/pnas.1900278116>, 2019a.
- 26 Magney, T. S., Frankenberg, C., Köhler, P., North, G., Davis, T. S., Dold, C., Dutta, D., Fisher, J. B., Grossmann, K., Harrington, A., Hatfield,
- 27 J., Stutz, J., Sun, Y., and Porcar-Castell, A.: Disentangling changes in the spectral shape of chlorophyll fluorescence: Implications for
- 28 remote sensing of photosynthesis, *Journal of Geophysical Research: Biogeosciences*, <https://doi.org/10.1029/2019jg005029>, 2019b.
- 29 Mahadevan, P., Wofsy, S. C., Matross, D. M., Xiao, X., Dunn, A. L., Lin, J. C., Gerbig, C., Munger, J. W., Chow, V. Y., and Gottlieb, E. W.: A
- 30 satellite-based biosphere parameterization for net ecosystem CO₂ exchange: Vegetation Photosynthesis and Respiration Model (VPRM),
- 31 *Global Biogeochemical Cycles*, 22, <https://doi.org/10.1029/2006gb002735>, 2008.
- 32 Mohammed, G. H., Colombo, R., Middleton, E. M., Rascher, U., van der Tol, C., Nedbal, L., Goulas, Y., Perez-Priego, O., Damm, A.,
- 33 Meroni, M., Joiner, J., Cogliati, S., Verhoef, W., Malenovsky, Z., Gastellu-Etchegorry, J.-P., Miller, J. R., Guanter, L., Moreno, J., Moya,
- 34 I., Berry, J. A., Frankenberg, C., and Zarco-Tejada, P. J.: Remote sensing of solar-induced chlorophyll fluorescence (SIF) in vegetation:
- 35 50 years of progress, *Remote Sensing of Environment*, 231, 111 177, <https://doi.org/10.1016/j.rse.2019.04.030>, 2019.
- 36 Monahan, A. H., Fyfe, J. C., Ambaum, M. H. P., Stephenson, D. B., and North, G. R.: Empirical Orthogonal Functions: The Medium is the
- 37 Message, *Journal of Climate*, 22, 6501–6514, <https://doi.org/10.1175/2009jcli3062.1>, 2009.
- 38 Monteith, J. L.: Solar Radiation and Productivity in Tropical Ecosystems, *Journal of Applied Ecology*, 9, 747–766, 1972.



- 1 Parazoo, N. C., Bowman, K., Fisher, J. B., Frankenberg, C., Jones, D. B., Cescatti, A., Perez-Priego, O., Wohlfahrt, G., and Montagnani,
2 L.: Terrestrial gross primary production inferred from satellite fluorescence and vegetation models, *Global change biology*, 20, 3103–21,
3 <https://doi.org/10.1111/gcb.12652>, 2014.
- 4 Parazoo, N. C., Arneeth, A., Pugh, T. A. M., Smith, B., Steiner, N., Luus, K., Commane, R., Benmergui, J., Stofferahn, E., Liu, J., Rodenbeck,
5 C., Kawa, R., Euskirchen, E., Zona, D., Arndt, K., Oechel, W., and Miller, C.: Spring photosynthetic onset and net CO₂ uptake in Alaska
6 triggered by landscape thawing, *Global change biology*, 24, 3416–3435, <https://doi.org/10.1111/gcb.14283>, 2018.
- 7 Parazoo, N. C., Frankenberg, C., Kohler, P., Joiner, J., Yoshida, Y., Magney, T., Sun, Y., and Yadav, V.: Towards a Harmo-
8 nized Long-Term Spaceborne Record of Far-Red Solar-Induced Fluorescence, *Journal of Geophysical Research: Biogeosciences*,
9 <https://doi.org/10.1029/2019jg005289>, 2019.
- 10 Peters, W., Jacobson, A. R., Sweeney, C., Andrews, A. E., Conway, T. J., Masarie, K., Miller, J. B., Bruhwiler, L. M., Petron, G., Hirsch, A. I.,
11 Worthy, D. E., van der Werf, G. R., Randerson, J. T., Wennberg, P. O., Krol, M. C., and Tans, P. P.: An atmospheric perspective on North
12 American carbon dioxide exchange: CarbonTracker, *Proc Natl Acad Sci*, 104, 18 925–30, <https://doi.org/10.1073/pnas.0708986104>, 2007.
- 13 Reichstein, M., Falge, E., Baldocchi, D., Papale, D., Aubinet, M., Berbigier, P., Bernhofer, C., Buchmann, N., Gilmanov, T., Granier, A.,
14 Grunwald, T., Havrankova, K., Ilvesniemi, H., Janous, D., Knohl, A., Laurila, T., Lohila, A., Loustau, D., Matteucci, G., Meyers, T.,
15 Miglietta, F., Ourcival, J.-M., Pumpanen, J., Rambal, S., Rotenberg, E., Sanz, M., Tenhunen, J., Seufert, G., Vaccari, F., Vesala, T., Yakir,
16 D., and Valentini, R.: On the separation of net ecosystem exchange into assimilation and ecosystem respiration: review and improved
17 algorithm, *Global change biology*, 11, 1424–1439, <https://doi.org/10.1111/j.1365-2486.2005.001002.x>, 2005.
- 18 Schaaf, C. B., Gao, F., Strahler, A. H., Lucht, W., Li, X., Tsang, T., Strugnell, N. C., Zhang, X., Jin, Y., Muller, J.-P., Lewis, P., Barns-
19 ley, M., Hobson, P., Disney, M., Roberts, G., Dunderdale, M., Doll, C., d’Entremont, R. P., Hu, B., Liang, S., Privette, J. L., and
20 Roy, D.: First operational BRDF, albedo nadir reflectance products from MODIS, *Remote Sensing of Environment*, 83, 135–148,
21 [https://doi.org/10.1016/s0034-4257\(02\)00091-3](https://doi.org/10.1016/s0034-4257(02)00091-3), 2002.
- 22 Sellers, P. J., Mintz, Y., Sud, Y. C., and Dalcher, A.: A Simple Biosphere Model (SIB) for Use within General Circulation Models, *Journal*
23 *of the Atmospheric Sciences*, 43, 505–531, [https://doi.org/10.1175/1520-0469\(1986\)043<0505:asbfmu>2.0.co;2](https://doi.org/10.1175/1520-0469(1986)043<0505:asbfmu>2.0.co;2), 1986.
- 24 Strahler, A., Muchoney, D., Borak, J., Friedl, F., Gopal, S., Lambin, L., and Moody, A.: MODIS Land Cover Product Algorithm Theoretical
25 Basis Document (ATBD), Tech. rep., Center for Remote Sensing, Department of Geography, Boston University, https://modis.gsfc.nasa.gov/data/atbd/atbd_mod12.pdf, 1999.
- 27 Sun, K., Zhu, L., Cady-Pereira, K., Chan Miller, C., Chance, K., Clarisse, L., Coheur, P.-F., Gonzalez Abad, G., Huang, G., Liu, X.,
28 Van Damme, M., Yang, K., and Zondlo, M.: A physics-based approach to oversample multi-satellite, multispecies observations to a
29 common grid, *Atmospheric Measurement Techniques*, 11, 6679–6701, <https://doi.org/10.5194/amt-11-6679-2018>, 2018a.
- 30 Sun, Y., Frankenberg, C., Wood, J. D., Schimel, D. S., Jung, M., Guanter, L., Drewry, D. T., Verma, M., Porcar-Castell, A., Griffis, T. J.,
31 Gu, L., Magney, T. S., Kohler, P., Evans, B., and Yuen, K.: OCO-2 advances photosynthesis observation from space via solar-induced
32 chlorophyll fluorescence, *Science*, 358, <https://doi.org/10.1126/science.aam5747>, 2017.
- 33 Sun, Y., Frankenberg, C., Jung, M., Joiner, J., Guanter, L., Köhler, P., and Magney, T.: Overview of Solar-Induced chlorophyll Fluorescence
34 (SIF) from the Orbiting Carbon Observatory-2: Retrieval, cross-mission comparison, and global monitoring for GPP, *Remote Sensing of*
35 *Environment*, 209, 808–823, <https://doi.org/10.1016/j.rse.2018.02.016>, 2018b.
- 36 Tans, P. P., Fung, I. Y., and Takahashi, T.: Observational constraints on the global atmospheric CO₂ budget, *Science*, 247, 1431–8,
37 <https://doi.org/10.1126/science.247.4949.1431>, 1990.



- 1 Tyler, C. M., Kuhn, B., and Davis, F. W.: Demography and recruitment limitations of three oak species in California, *Q Rev Biol*, 81, 127–52,
2 2006.
- 3 University of California at Davis: Rice Production Manual, Tech. rep., California Rice Production Workshop, Davis, CA, <http://rice.ucanr.edu/files/288581.pdf>, 2018.
- 4
- 5 USDA: National Agricultural Statistics Service Cropland Data Layer: Published crop-specific data layer, <https://nassgeodata.gmu.edu/CropScape/>, 2018.
- 6
- 7 USGCRP: Second State of the Carbon Cycle Report (SOCCR2): A Sustained Assessment Report, Tech. rep., U.S. Global Change Research
8 Program, <https://doi.org/10.7930/SOCCR2.2018>, 2018.
- 9 Veefkind, J. P., Aben, I., McMullan, K., Förster, H., de Vries, J., Otter, G., Claas, J., Eskes, H. J., de Haan, J. F., Kleipool, Q., van Weele,
10 M., Hasekamp, O., Hoogeveen, R., Landgraf, J., Snel, R., Tol, P., Ingmann, P., Voors, R., Kruizinga, B., Vink, R., Visser, H., and Levelt,
11 P. F.: TROPOMI on the ESA Sentinel-5 Precursor: A GMES mission for global observations of the atmospheric composition for climate,
12 air quality and ozone layer applications, *Proc SPIE*, 120, 70–83, <https://doi.org/10.1016/j.rse.2011.09.027>, 2012.
- 13 Walther, S., Voigt, M., Thum, T., Gonsamo, A., Zhang, Y., Kohler, P., Jung, M., Varlagin, A., and Guanter, L.: Satellite chlorophyll fluores-
14 cence measurements reveal large-scale decoupling of photosynthesis and greenness dynamics in boreal evergreen forests, *Global change*
15 *biology*, 22, 2979–96, <https://doi.org/10.1111/gcb.13200>, 2016.
- 16 Xu, L. and Baldocchi, D. D.: Seasonal trends in photosynthetic parameters and stomatal conductance of blue oak (*Quercus douglasii*) under
17 prolonged summer drought and high temperature, *Tree Physiol*, 23, 865–77, <https://doi.org/10.1093/treephys/23.13.865>, 2003.
- 18 Xu, L. and Baldocchi, D. D.: Seasonal variation in carbon dioxide exchange over a Mediterranean annual grassland in California, *Agricultural*
19 *and Forest Meteorology*, 123, 79–96, <https://doi.org/10.1016/j.agrformet.2003.10.004>, 2004.
- 20 Xu, L., Baldocchi, D. D., and Tang, J.: How soil moisture, rain pulses, and growth alter the response of ecosystem respiration to temperature,
21 *Global Biogeochemical Cycles*, 18, <https://doi.org/10.1029/2004gb002281>, 2004.
- 22 Yang, H., Yang, X., Zhang, Y., Heskell, M. A., Lu, X., Munger, J. W., Sun, S., and Tang, J.: Chlorophyll fluorescence tracks seasonal variations
23 of photosynthesis from leaf to canopy in a temperate forest, *Global change biology*, 23, 2874–2886, <https://doi.org/10.1111/gcb.13590>,
24 2017.
- 25 Yang, K., Ryu, Y., Dechant, B., Berry, J. A., Hwang, Y., Jiang, C., Kang, M., Kim, J., Kimm, H., Kornfeld, A., and Yang, X.: Sun-induced
26 chlorophyll fluorescence is more strongly related to absorbed light than to photosynthesis at half-hourly resolution in a rice paddy, *Remote*
27 *Sensing of Environment*, 216, 658–673, <https://doi.org/10.1016/j.rse.2018.07.008>, 2018.
- 28 Yang, P. and van der Tol, C.: Linking canopy scattering of far-red sun-induced chlorophyll fluorescence with reflectance, *Remote Sensing of*
29 *Environment*, 209, 456–467, <https://doi.org/10.1016/j.rse.2018.02.029>, 2018.
- 30 Yang, X., Tang, J., Mustard, J. F., Lee, J.-E., Rossini, M., Joiner, J., Munger, J. W., Kornfeld, A., and Richardson, A. D.: Solar-induced chloro-
31 phyll fluorescence that correlates with canopy photosynthesis on diurnal and seasonal scales in a temperate deciduous forest, *Geophysical*
32 *Research Letters*, 42, 2977–2987, <https://doi.org/10.1002/2015gl063201>, 2015.
- 33 Yu, L., Wen, J., Chang, C. Y., Frankenberg, C., and Sun, Y.: High-Resolution Global Contiguous SIF of OCO-2, *Geophysical Research*
34 *Letters*, 46, 1449–1458, <https://doi.org/10.1029/2018gl081109>, 2019.
- 35 Zeng, Y., Badgkey, G., Dechant, B., Ryu, Y., Chen, M., and Berry, J. A.: A practical approach for estimating the escape ratio of near-infrared
36 solar-induced chlorophyll fluorescence, *Remote Sensing of Environment*, XX, <https://doi.org/10.1016/j.rse.2019.05.028>, 2019.
- 37 Zhang, Y., Joiner, J., Alemohammad, S. H., Zhou, S., and Gentine, P.: A global spatially contiguous solar-induced fluorescence (CSIF)
38 dataset using neural networks, *Biogeosciences*, 15, 5779–5800, <https://doi.org/10.5194/bg-15-5779-2018>, 2018.



- 1 Zhu, L., Jacob, D. J., Mickley, L. J., Marais, E. A., Cohan, D. S., Yoshida, Y., Duncan, B. N., Gonzalez Abad, G., and Chance, K. V.:
2 Anthropogenic emissions of highly reactive volatile organic compounds in eastern Texas inferred from oversampling of satellite (OMI)
3 measurements of HCHO columns, *Environmental Research Letters*, 9, 114 004, <https://doi.org/10.1088/1748-9326/9/11/114004>, 2014.
- 4 Zoogman, P., Liu, X., Suleiman, R. M., Pennington, W. F., Flittner, D. E., Al-Saadi, J. A., Hilton, B. B., Nicks, D. K., Newchurch, M. J., Carr,
5 J. L., Janz, S. J., Andraschko, M. R., Arola, A., Baker, B. D., Canova, B. P., Chan Miller, C., Cohen, R. C., Davis, J. E., Dussault, M. E.,
6 Edwards, D. P., Fishman, J., Ghulam, A., Gonzalez Abad, G., Grutter, M., Herman, J. R., Houck, J., Jacob, D. J., Joiner, J., Kerridge, B. J.,
7 Kim, J., Krotkov, N. A., Lamsal, L., Li, C., Lindfors, A., Martin, R. V., McElroy, C. T., McLinden, C., Natraj, V., Neil, D. O., Nowlan,
8 C. R., O'Sullivan, E. J., Palmer, P. I., Pierce, R. B., Pippin, M. R., Saiz-Lopez, A., Spurr, R. J. D., Szykman, J. J., Torres, O., Veefkind, J. P.,
9 Veihelmann, B., Wang, H., Wang, J., and Chance, K.: Tropospheric emissions: Monitoring of pollution (TEMPO), *Journal of Quantitative*
10 *Spectroscopy and Radiative Transfer*, 186, 17–39, <https://doi.org/10.1016/j.jqsrt.2016.05.008>, 2017.
- 11 Zuromski, L. M., Bowling, D. R., Köhler, P., Frankenberg, C., Goulden, M. L., Blanken, P. D., and Lin, J. C.: Solar-Induced Fluorescence
12 Detects Interannual Variation in Gross Primary Production of Coniferous Forests in the Western United States, *Geophysical Research*
13 *Letters*, 45, 7184–7193, <https://doi.org/10.1029/2018gl077906>, 2018.